



TECHNISCHE  
UNIVERSITÄT  
WIEN



## Diploma thesis

Effects of turbofan engine nozzle flows on nozzle  
pressure coefficients in a high-lift aircraft  
configuration

carried out for the purpose of obtaining the degree of **Diplom-Ingenieur**  
(Dipl.-Ing. or DI) under the supervision of

**Prof. Dr.-Ing. Martin Berens**

(Institute of Engineering Design and Product Development)

as well as under the supervision of

**Univ.Ass. Marcos Vitor De Rosa Jacinto da Silva,**  
**Eng.Aeronautico**

(Institute of Engineering Design and Product Development)

submitted at TU Wien

**Faculty of Mechanical and Industrial Engineering**

**Lukas Nikolaus Steininger, BSc**

11771151

(066 445)

I acknowledge that I am only permitted to publish my thesis under the designation

## Diploma thesis

with the approval of the examination committee.

### *Statutory Declaration*

I hereby declare under oath that the present thesis was prepared independently by myself in accordance with the recognized principles of academic writing. All resources used, particularly the literature consulted, are cited and listed in the thesis. Passages taken verbatim from other sources are clearly identified as such.

The topic of this thesis has not previously been submitted, either in Austria or abroad, to any examiner for evaluation in any form as part of an examination. This thesis corresponds in its entirety to the version evaluated by the examiners.

Wien, Dezember 2025

---

Lukas Nikolaus Steininger BSc

## Abstract

In order to increase the propulsive efficiency of a turbofan engine, the fan pressure ratio (FPR) needs to be lowered. To maintain constant thrust, this requires an increased bypass ratio. When performing in-flight thrust and drag measurements, the static pressure field can influence the engine operating characteristics, which, under the assumptions made during measurements, can lead to a bias error in the thrust-drag book keeping. Using CFD analysis on the Common Research Model - High Lift (CRM-HL), this bias error is quantified for both a Through-Flow Nacelle (TFN) and Turbofan Propulsion Simulator (TPS) for a variety of angles of attack and FPRs. The results show a clear sensitivity of the bias error for both variables. Finally, recommendations for improved measurements during book keeping to avoid this bias error are made.

# Contents

<b>1</b>	<b>Introduction</b>	<b>4</b>
1.1	Motivation . . . . .	4
1.2	High-bypass turbofan engines . . . . .	5
<b>2</b>	<b>Thrust and drag book keeping</b>	<b>8</b>
2.1	Definitions . . . . .	8
2.2	Single-stream engine thrust . . . . .	9
2.3	Dual-Stream engine thrust . . . . .	11
2.4	Thrust calculation using nozzle coefficients . . . . .	13
2.4.1	Ideal nozzle . . . . .	13
2.4.2	Nozzle coefficients . . . . .	14
2.4.3	Thrust calculation . . . . .	15
2.5	Systematic errors within the book keeping . . . . .	15
2.5.1	Mismatch of physical and model engine power . . . . .	15
2.5.2	Nozzle suppression coefficient . . . . .	18
<b>3</b>	<b>CFD methodology</b>	<b>20</b>
3.1	Geometry . . . . .	20
3.1.1	Common Research Model . . . . .	20
3.1.2	CFD Model Geometry . . . . .	21
3.1.3	TPS model geometry . . . . .	23
3.2	General parameters . . . . .	27
3.2.1	Domain . . . . .	27
3.2.2	Solvers . . . . .	27
3.3	TPS model . . . . .	28
3.4	Mesh . . . . .	30
3.4.1	General setup . . . . .	30
3.4.2	Mesh independence study . . . . .	32
3.5	Model verification . . . . .	36
<b>4</b>	<b>Suppression effect analysis</b>	<b>39</b>
4.1	Impact of Angle of Attack for a TFN . . . . .	39
4.2	Impact of Angle of Attack for a TPS . . . . .	44
4.3	Impact of thrust rating . . . . .	46
4.4	Improvements to the book keeping strategy . . . . .	50
<b>5</b>	<b>Conclusions and recommendations</b>	<b>52</b>
5.1	Conclusions . . . . .	52
5.2	Recommendations . . . . .	53

<b>List of Figures</b>	<b>54</b>
<b>List of Tables</b>	<b>56</b>
<b>Bibliography</b>	<b>57</b>

# Nomenclature

$\gamma$	Heat capacity ratio
$\phi_{AB}$	Afterbody force
$\phi_{ADD}$	Additive drag force
$\phi_{IC}$	Inlet-Cowl forebody force
$\phi_{PLUG}$	Plug force
$\phi_{PYLON}$	Pylon force
$A$	Cross section area
$A_i$	Cross section area at engine station $i$
$C_D$	Flow / Discharge coefficient
$c_L$	Lift coefficient
$c_P$	Pressure coefficient
$C_V$	Specific thrust / Velocity coefficient
$C_{Ref}$	Reference aerodynamic chord
$CpC$	Cells per Chord
$CRM$	Common Research Model
$CRM - HL$	Common Research Model - High Lift
$D_{AFS}$	Airframe system drag
$F_G$	Gross thrust
$F_G^*$	Modified gross thrust
$F_N$	Net thrust
$F_N^*$	Modified net thrust

---

$F_{EX}$	Excess thrust
$F_{IPF}$	Installed propulsive force
$F_{SE}$	Static equilibrium force
$FNPR$	Fan nozzle pressure ratio
$Ma$	Mach number
$P_S$	Static pressure
$P_{Si}$	Static pressure at engine station i
$PR$	Nozzle pressure ratio
$q_0$	Free stream dynamic pressure
$R_n$	Nominal Reynolds number
$T_{ti}$	Total temperature at engine station i
$V_0$	Free stream velocity
$V_i$	Velocity at engine station i
$W_0$	Free stream air mass flow
$W_i$	Air mass flow at engine station i
$V_j$	Jet velocity
$W$	Air mass flow

# 1 Introduction

## 1.1 Motivation

With the impact of emissions on the climate increasing in importance over the past decades, the aviation industry has come under scrutiny. In 2017, the aviation industry emitted 13.9% of the overall EU transport greenhouse gas emissions [1], with multiple agencies predicting a doubling of the greenhouse gas emissions by 2050 [2]. This increase has been primarily driven by the increase in air traffic. From 2000 to 2019, just ahead of the COVID-19 pandemic, the number of passengers increased globally from 1.8 billion to 4.6 billion per year [3], with an average annual rate of around 5% [4]. This increase in air traffic grows at a greater rate than aircraft improvements in terms of fuel consumption and greenhouse gas emissions. Given the EU's goal of zero net greenhouse gas emissions by the year 2050 [5], the aviation industry is motivated to reduce fuel consumption.

Additionally, fuel is one of the cost drivers in modern aircraft, making up around 24.7% of an airline's cost structure [6]. This is further amplified by the recent volatility of the crude oil price, seen in figure 1.1, which leads to increased difficulty in predicting an airline's financial performance.

The vertical and longitudinal dynamics of an aircraft are dominated by four forces - lift, weight, drag and thrust. In steady-state flight, the sum of lift and weight and respectively thrust and drag is zero. The combination of these parameters allows to provide a good estimate for the overall performance characteristics of an aircraft. Reduced drag and weight lead to reduced thrust and lift requirements, which increases the efficiency of an aircraft and thus lowers the operating cost and environmental impact.

However, while weight and thus lift can be determined easily, determining drag and thrust is more challenging. This is because actually measuring drag and thrust in flight is inherently difficult. Drag is the sum of all pressure and shear forces acting on the entire aircraft. Obtaining this information through experimental data, particularly during in-flight testing, is difficult and frequently requires well calibrated models and additional assumptions. The thrust, physically, results from an increase in air momentum of the air going through the engine in reference to the ambient freestream air. This airstream is hard to measure without introducing blockage artifacts which can skew the results. As a consequence, thrust-drag book keeping is performed using a combination of calibration facility testing and in-flight measurements [8].

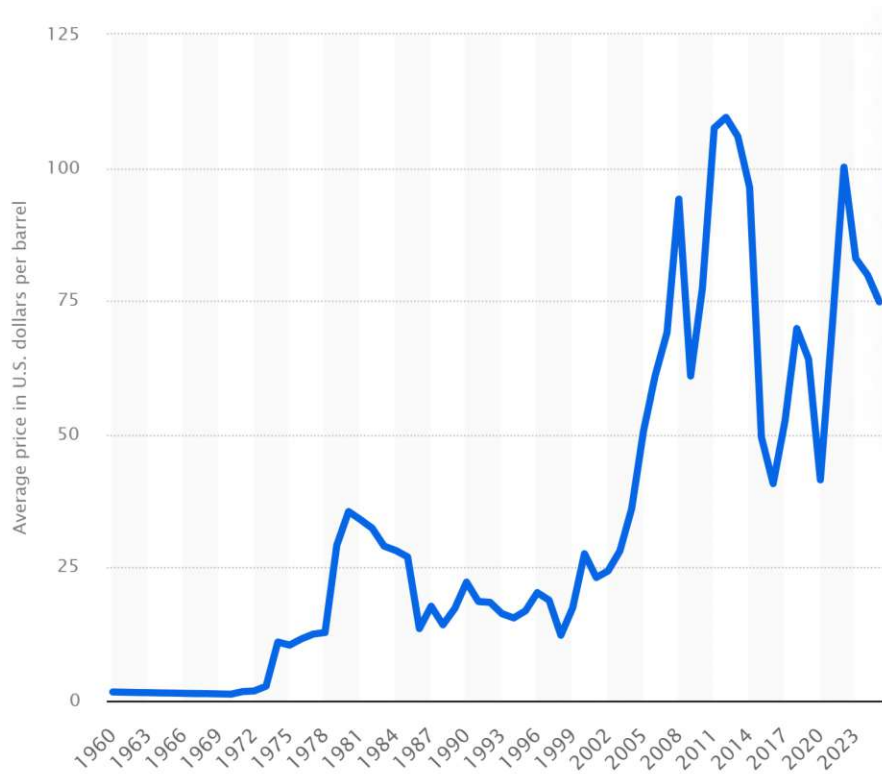


Figure 1.1: Crude oil price development from 1960 to 2025 (Source: [7])

## 1.2 High-bypass turbofan engines

In order to minimize fuel consumption, the efficiency of the aircraft must be increased. This can stem from improvements in aerodynamic efficiency, mass reductions, or propulsion efficiency. The latter has resulted in significant efficiency improvements over the past decades [9].

The efficiency of a turbofan propulsion system is dominated by the thermal efficiency of the cycle  $\eta_{thermal}$  and the propulsive efficiency  $\eta_p$ . The thermal efficiency describes the efficiency of transferring thermal energy within the fuel into kinetic jet energy. The propulsive efficiency describes the transfer of kinetic power within the exhaust jet into useful thrust power [9]. The kinetic power can be defined as:

$$P_{kin,delta} = \frac{1}{2} W_0 (V_j^2 - V_0^2) \quad (1.1)$$

where  $V_j$  is the jet velocity,  $V_0$  is the freestream velocity, and  $W_0$  is the freestream mass flow. The propulsive efficiency can thus be defined as:

$$\eta_p = \frac{W_0(V_j - V_0)V_0}{\frac{1}{2}W_0(V_j^2 - V_0^2)} = \frac{2}{\frac{V_j}{V_0} + 1} \quad (1.2)$$

As can be seen from equation 1.2, high propulsive efficiency promotes reducing the ratio of  $\frac{V_j}{V_0}$  towards 1. However, the strive for reduced jet velocities has an impact on the net thrust  $F_N$ :

$$F_N = W_0(V_j - V_0) \quad (1.3)$$

This shows that simply reducing the jet velocity will also reduce thrust. Thus, in order to maintain a consistent thrust level, the mass flow  $W_0$  needs to be increased. This requires increasing the fan flow area. However, doing so results in additional undesirable effects, such as an increase in weight, cost and drag. The combined effect of these parameters can be seen in figure 1.2.

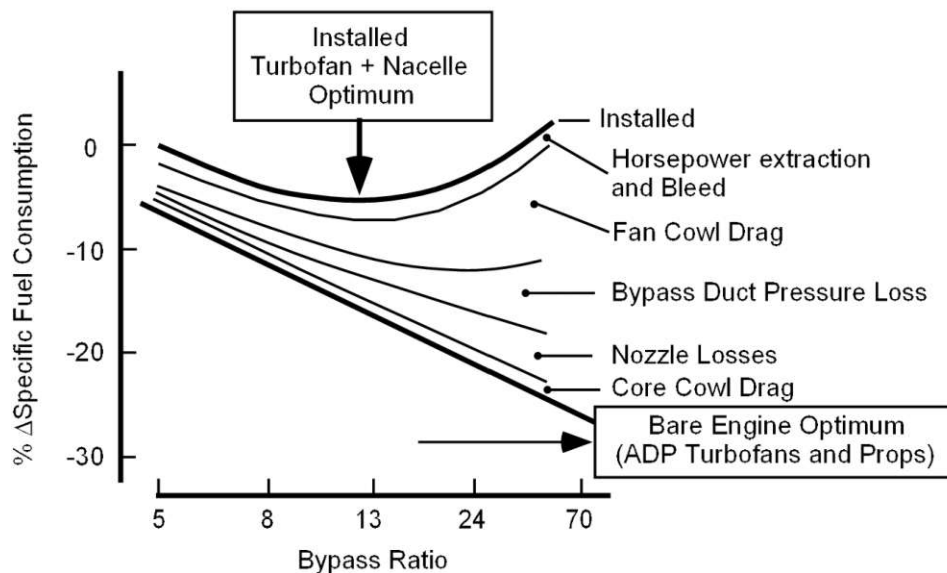


Figure 1.2: Turbofan engine and nacelle installation SFC increments (Source: [9])

Through technological advancements, the minimum of the curve has continuously shifted towards higher bypass ratios [9]. This trend, however, leads to increased sensitivity of the fan characteristics due to its reduced fan nozzle pressure ratio [10]. In particular, the gross to net thrust ratio increases significantly with higher bypass ratios, increasing cruise sensitivity. DeWolf noted that changes in the local pressure field induced by the presence of wings can lead to an incorrect prediction of the effective nozzle pressure ratio, which can lead to an incorrect bookkeeping of the net thrust. In this thesis, this effect will be referred to as flow suppression [11]. This effect reaches its maximum effect for intermediate subsonic Mach numbers of around 0.5 [10]. Additionally, when high-lift configurations are employed for take-off and landing, the increased circulation of the

wing increases the high pressure field under the wing and around the engine, which potentially increases suppression effects.

The aim of this work is to investigate the impact of the wing induced flow suppression on the engine for a high-lift configuration. This is investigated using the Common Research Model - High Lift (CRM-HL) as a reference geometry, with the fan nozzle pressure calculated using Computational Fluid Dynamics (CFD). The flow suppression characteristics of two engine models that are currently employed in wind tunnels are mutually compared - a flow-through nacelle, and a TPS model.

## 2 Thrust and drag book keeping

### 2.1 Definitions

Before investigating drag and thrust, it is necessary to define control locations along the flow paths of a dual – stream turbofan engine. The structure proposed by SAE AIR1703A is seen in Figure 2.1 [12]. Single digit numbers indicate the flow through the engine core, whereas double digit numbers indicated flow through the bypass duct.

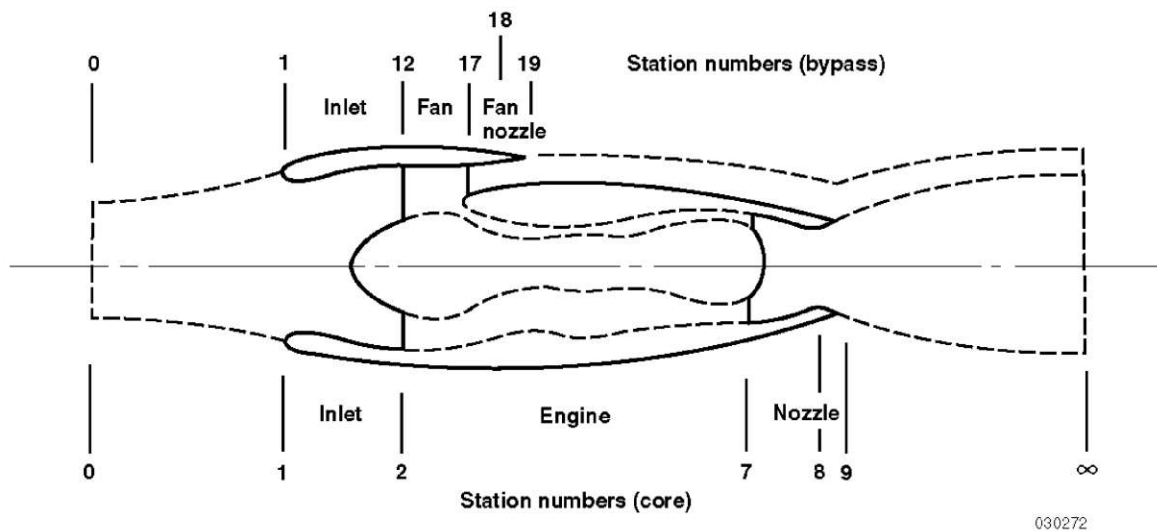


Figure 2.1: Station positions and labels for a turbofan engine (Source: [12])

In order to start off with the determination of thrust, the excess thrust  $F_{EX}$  is defined as the difference between the installed propulsive force  $F_{IPF}$  and the airframe system drag  $D_{AFS}$ :

$$F_{EX} = F_{IPF} - D_{AFS} \quad (2.1)$$

In level, non-accelerating flight, the thrust force and drag force are equal:

$$F_{IPF} = D_{AFS} \quad (2.2)$$

The sum of all forces  $\Sigma F$  for steady flows can be described by the change of momentum, which is a function of mass flow  $W$  and velocity  $V$ . The macroscopic momentum balance results in:

$$\Delta(WV) = \Sigma F \quad (2.3)$$

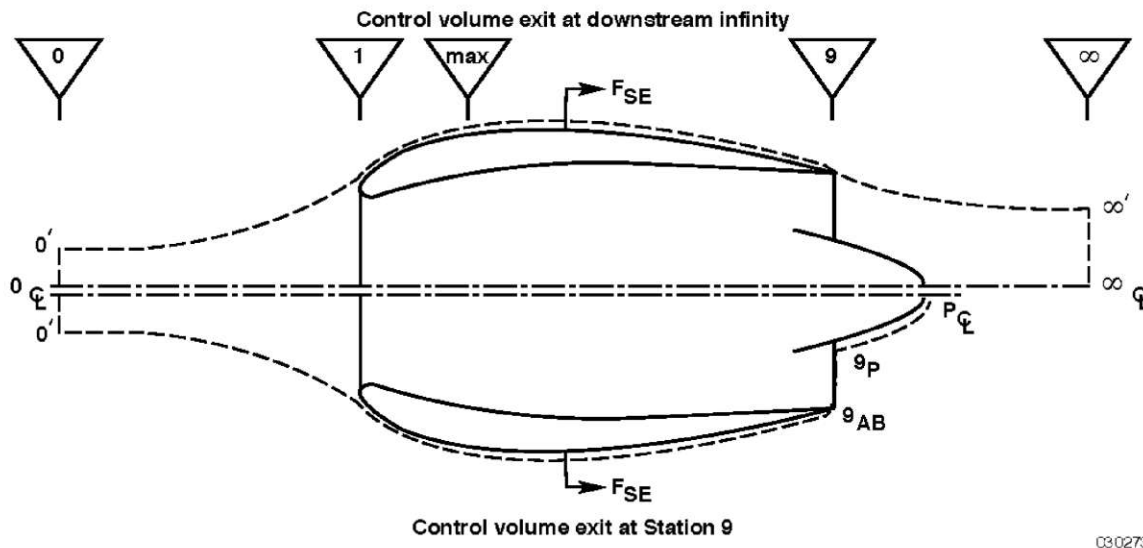
Neglecting viscous forces acting tangentially to the surfaces, the sum of all forces can be expressed as:

$$\Sigma F = \Sigma \int p dA + F_{SE} \quad (2.4)$$

where  $F_{SE}$  acts as the force that keeps the control volume in static equilibrium. Assuming uniform static pressure, the integrals can be expressed as:

$$\int p dA = pA \quad (2.5)$$

## 2.2 Single-stream engine thrust



030273

Figure 2.2: Control positions for a single - stream engine (Source: [12])

AIR1703A provides two definitions for control boundaries on a single-stream engine. The chosen method is using the control boundaries shown in the lower half of Figure 2.2. Here, station 9 is defined as the exit boundary for the flow around the engine, leading to the momentum balance:

$$W_9V_9 - W_0V_0 = \int_{0_{cL}}^{0'} P_S dA + \int_{0'}^1 P_S dA + \int_1^{max} P_S dA + \int_{max}^{9_{AB}} P_S dA + \int_{9_{AB}}^{9_P} P_S dA + \int_{9_P}^{P_{cL}} P_S dA + F_{SE} \quad (2.6)$$

Assuming uniform pressure, the following integrals can be simplified:

$$\int_{0_{cL}}^{0'} P_S dA = P_{S0}A_0 \quad (2.7)$$

$$\int_{9_P}^{P_{cL}} P_S dA = -P_{S9}A_9 \quad (2.8)$$

Which leads to:

$$F_{IPF} = -W_0V_0 - P_{S0}A_0 - \int_{0'}^1 P_S dA - \int_1^{max} P_S dA - \int_{max}^{9_{AB}} P_S dA - \int_{9_P}^{P_{cL}} P_S dA + W_9V_9 + P_{S9}A_9 \quad (2.9)$$

The pressure forces can be referred to ambient pressure. This is achieved by adding  $P_{S0}A_{max}$  to the right side of equation 2.9 in the form of:

$$P_{S0}A_{max} = P_{S0}A_0 + \int_{0'}^1 P_{S0} dA + \int_1^{max} P_{S0} dA \quad (2.10)$$

and subtracting it from the right side in the form of:

$$-P_{S0}A_{max} = - \int_{max}^{9_{AB}} P_{S0} dA - \int_{9_P}^{P_{cL}} P_{S0} dA - P_{S0}A_9 \quad (2.11)$$

This results in:

$$F_{IPF} = -W_0V_0 - \phi_{ADD} - \phi_{IC} + \phi_{AB} + \phi_{PLUG} + W_9V_9 + (P_{S9} - P_{S0})A_9 \quad (2.12)$$

with the Additive Drag Force  $\phi_{ADD}$ :

$$\phi_{ADD} = \int_0^1 (P_S - P_{S0}) dA \quad (2.13)$$

the Inlet-Cowl Forebody Force  $\phi_{IC}$ :

$$\phi_{IC} = \int_1^{max} (P_S - P_{S0})dA \quad (2.14)$$

the Afterbody Force  $\phi_{AB}$ :

$$\phi_{AB} = - \int_{max}^9 (P_S - P_{S0})dA \quad (2.15)$$

and the Plug Force  $\phi_{PLUG}$ :

$$\phi_{PLUG} = \int_{9P}^{P_{cL}} (P_S - P_{S0})dA \quad (2.16)$$

Taking  $F_{IPF}$  and ignoring ram drag, inlet spillage drag and Nozzle Thrust-Minus-Drag force, the gross thrust is obtained:

$$F_G = F_{IPF} + W_0V_0 + \phi_{ADD} + \phi_{IC} - \phi_{AB} - \phi_{PLUG} = W_9V_9 + (P_{S9} - P_{S0})A_9 \quad (2.17)$$

The modified gross thrust takes the plug force into account:

$$F_G^* = W_9V_9 + (P_{S9} - P_{S0})A_9 + \phi_{PLUG} \quad (2.18)$$

Subtracting the ram drag  $W_0V_0$  from the modified gross thrust  $F_G^*$  results in the modified net thrust  $F_N^*$ :

$$F_N^* = W_9V_9 + (P_{S9} - P_{S0})A_9 + \phi_{PLUG} - W_0V_0 \quad (2.19)$$

## 2.3 Dual-Stream engine thrust

The control domains for a dual stream engine are shown in Figure 2.3. Using a similar approach, for a dual-stream engine, the Installed Propulsive Force  $F_{IPF}$  can be expressed as:

$$F_{IPF} = -W_0V_0 - \phi_{ADD} - \phi_{IC} + \phi_{FCAB} + W_9V_9 + (P_{S9} - P_{S0})A_9 + \phi_{PLUG} \\ + W_{19}V_{19} + (P_{S19} - P_{S0})A_{19} + \phi_{CCAB} + \phi_{PYLON} \quad (2.20)$$

with:

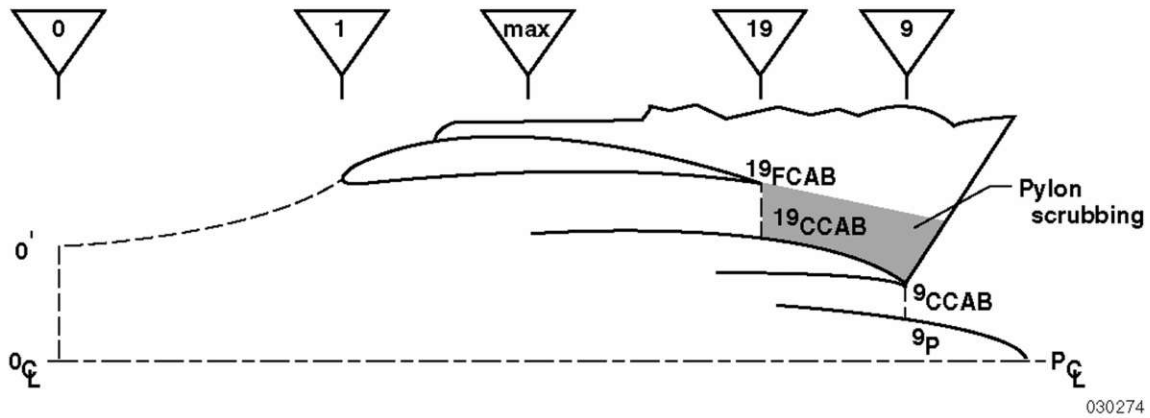


Figure 2.3: Control positions for a dual - stream engine (Source: [12])

$$\phi_{ADD} = \int_{0'}^1 P_S dA \quad (2.21)$$

$$\phi_{IC} = \int_1^{max} P_S dA \quad (2.22)$$

$$\phi_{FCAB} = - \int_{max}^{19FCAB} P_S dA \quad (2.23)$$

$$\phi_{CCAB} = - \int_{19CCAB}^{9CCAB} P_S dA \quad (2.24)$$

$$\phi_{PLUG} = - \int_{9P}^{9cL} P_S dA \quad (2.25)$$

$$\phi_{PYLON} = - \int_{PYLON} P_S dA \quad (2.26)$$

The gross thrust  $F_G$  is thus computed as:

$$F_G = W_9 V_9 + (P_{S9} - P_{S0}) A_9 + W_{19} V_{19} + (P_{S19} - P_{S0}) A_{19} \quad (2.27)$$

## 2.4 Thrust calculation using nozzle coefficients

The established convention necessitates the knowledge of pressure, mass flow and velocity for all exit sections. While theoretically possible, this would involve probes on rigs which cause significant interference with the airflow, altering the result. Instead, the airflow is calculated by exploiting the well-known nozzle geometry and its physical behaviour. As previously described, the thrust applies at the nozzle section, which allows for the calculation of in-flight thrust and mass flow [12]. This method will now be described.

### 2.4.1 Ideal nozzle

To provide a better understanding of nozzle behaviour, the nozzle geometry is split into three stations. The nozzle entry plane is defined as station 7, the minimum throat area is defined as station 8, and the nozzle exit plane is defined as station 9.

The method relies on the assumption of an ideal nozzle. This involves the assumption of one-dimensional, isentropic flow downstream of the nozzle entry plane. An ideal nozzle achieves sonic conditions at the critical operating condition. For subcritical conditions, the pressure is assumed to be equal to the ambient static pressure  $P_{S0}$ . This behaviour is identical for convergent and convergent-divergent nozzles. During supercritical operation,  $P_{S9}$  will exceed  $P_{S0}$ , with the convergent-divergent nozzle delivering increased thrust due to isentropic expansion. As an ideal nozzle is assumed to be adiabatic and lossless, the total temperature, total pressure and mass flow remain constant throughout the nozzle. [12].

Ideal nozzle flow and thrust can be expressed using three non-dimensional functions:

$$\left[ W\sqrt{RT_T} \right]_{ID} = \text{Flow function} \quad (2.28)$$

$$\left[ F_G/AP_{S0} \right]_{ID} = \text{Thrust function} \quad (2.29)$$

$$\left[ F_G/W\sqrt{RT_T} \right]_{ID} = \text{Specific Thrust function} \quad (2.30)$$

These functions are related by:

$$\left[ F_G/AP_{S0} \right]_{ID} = \left[ W\sqrt{RT_T} \right]_{ID} \left[ F_G/W\sqrt{RT_T} \right]_{ID} \left[ P_T/P_{S0} \right] \quad (2.31)$$

The mass flow for an ideal nozzle is defined as [9]:

$$W_{id} = \left( \frac{P_{S0}}{P_t} \right)^{\frac{1}{\gamma}} \cdot \sqrt{\frac{2\gamma}{R(\gamma-1)} \cdot \left[ 1 - \left( \frac{P_{S0}}{P_t} \right)^{\frac{\gamma-1}{\gamma}} \right]} \cdot \frac{A \cdot P_t}{\sqrt{T_t}} \quad (2.32)$$

## 2.4.2 Nozzle coefficients

As actual nozzle performance deviates from ideal nozzle performance, nozzle coefficients are established to provide physical measures to relate them in context for thrust determination.

The discharge coefficient  $C_D$  is defined as the ratio of actual to ideal mass flow:

$$C_{D,8} = \frac{W_{ACT}}{W_{ID}} \quad (2.33)$$

If the Mach numbers are equal, it can also be interpreted as the ratio of the effective area to the physical area:

$$C_D = \frac{A_{8,EFF}}{A_8} \quad (2.34)$$

The specific thrust coefficient  $C_V$  is defined as the ratio of the actual specific thrust to the ideal specific thrust:

$$C_V = \frac{(F_G/W)_{ACT}}{(F_G/W)_{ID,CON-DI}} \quad (2.35)$$

It can also be interpreted as a ratio of the effective velocity to the ideal velocity:

$$C_V = \frac{V_{9,EFF}}{V_{9,ID,CON-DI}} \quad (2.36)$$

This allows to compute the actual gross thrust:

$$F_{G,ACT} = C_V \cdot W_{ACT} \cdot V_{9,ID,CON-DI} \quad (2.37)$$

### 2.4.3 Thrust calculation

Using the established nozzle models, the bypass thrust can now be computed [9]:

$$F_{G,19} = C_{V,17} \cdot \left[ \frac{F}{W\sqrt{T}} \right]_{17,id} \cdot W_{17} \cdot \sqrt{T_{t17}} \quad (2.38)$$

with the mass flow for an unchoked nozzle:

$$W_{17,id} = \left( \frac{P_{S0}}{P_{t17}} \right)^{\frac{1}{\gamma}} \cdot \sqrt{\frac{2\gamma}{R(\gamma-1)} \left[ 1 - \left( \frac{P_{S0}}{P_{t17}} \right)^{\left( \frac{\gamma-1}{\gamma} \right)} \right]} \cdot \frac{A_{18} \cdot P_{t17}}{\sqrt{T_{t17}}} \quad (2.39)$$

the bypass specific thrust function (equivalent to  $\frac{V_{17}}{\sqrt{T_{t17}}}$ ):

$$\left[ \frac{F}{W\sqrt{T}} \right]_{17,id} = \sqrt{\frac{2\gamma R}{(\gamma-1)} \left[ 1 - \left( \frac{P_{S0}}{P_{t17}} \right)^{\left( \frac{\gamma-1}{\gamma} \right)} \right]} \quad (2.40)$$

and the actual mass flow rate:

$$W_{17} = W_{17,id} \cdot C_{D,17} \quad (2.41)$$

Defining the fan nozzle pressure ratio as  $FNPR = \frac{P_{t17}}{P_{S0}}$ , the equation can be contracted to:

$$F_{G,19} = C_{V,17} \cdot C_{D,17} \cdot FNPR^{-\frac{1}{\gamma}} \frac{2\gamma}{\gamma-1} \left[ 1 - FNPR^{\frac{1-\gamma}{\gamma}} \right] \cdot A_{18} \cdot P_{t17} \quad (2.42)$$

## 2.5 Systematic errors within the book keeping

### 2.5.1 Mismatch of physical and model engine power

The book keeping of thrust and drag relies heavily on the assumption of an ideal nozzle. While this includes minor non-physicalities such as the assumption of isentropic flow which neglects viscous effects within the boundary layer, the main issue lies within the assumption of the exit static pressure being equal to the freestream static pressure.

Using the freestream dynamic pressure  $q_0$ , the actual nozzle exit static pressure can be expressed by a pressure coefficient:

$$c_{P,19} = \frac{P_{S19,ACT} - P_{S0}}{q_0} \quad (2.43)$$

This allows to define the ratio of the actual nozzle exit static pressure to the freestream static pressure as:

$$\frac{P_{S19,ACT}}{P_{S0}} = 1 + \frac{1}{2} \cdot c_P \cdot \gamma \cdot Ma^2 \quad (2.44)$$

The nozzle pressure ratio can be adjusted to  $PR = FNPR \cdot \frac{P_0}{P_{19,ACT}}$ . This has an impact on the fan mass flow:

$$W_{17} = C_{D,17} \cdot (PR)^{-\frac{1}{\gamma}} \cdot \sqrt{\frac{2\gamma}{R(\gamma-1)} \left[ 1 - (PR)^{\left(\frac{1-\gamma}{\gamma}\right)} \right]} \cdot \frac{A_{18} \cdot P_{t17}}{\sqrt{T_{t17}}} \quad (2.45)$$

The velocity is altered as well, as the pressure ratio is now reduced. In addition to that, referring to equation 2.27, an additional pressure term  $(P_{S19} - P_{S0})A_{19}$  is introduced. To alleviate both of these problems, the downstream reference area for the momentum balance is changed to position  $\infty$ . This position is characterized by freestream static pressure, which, in combination with the assumption of isentropic flow, results in the velocity  $V_\infty$  being driven only by the FNPR.

With the reduced mass flow passing through the fan stage, engine operation changes. As the turbine is usually unaffected by flow suppression, the fan shaft power stays constant. As a result, the fan operation shifts towards lower mass flows, but higher FPRs. This effect can be schematically seen in Figure 2.4:

Common measurement techniques, however, only capture the total temperature and total pressure of the flow behind the fan stage, although SAE AIR5450 does include a discussion about nozzle static pressure measurements [9]. The mass flow calculation is then based on unsuppressed nozzle flow, which does not take the physical effects of flow suppression, namely the increased total pressure, total temperature and nozzle exit static pressure, into account. This results in the calculated operating point being in excess of the true engine power, which is unphysical. This is demonstrated in Figure 2.5.

Since in steady-state flight, drag and thrust are balanced, this excess in thrust is instead being wrongly attributed to the airframe drag during book keeping, while the thrust of the engine is incorrectly inflated. For validation and measurement purposes, this leads to a substantial error in drag and thrust prediction.

In conclusion, the error in the thrust-drag book keeping arises from neglecting the impact of the nozzle exit static pressure onto the mass flow, which leads to an overestimation of engine power and thrust.

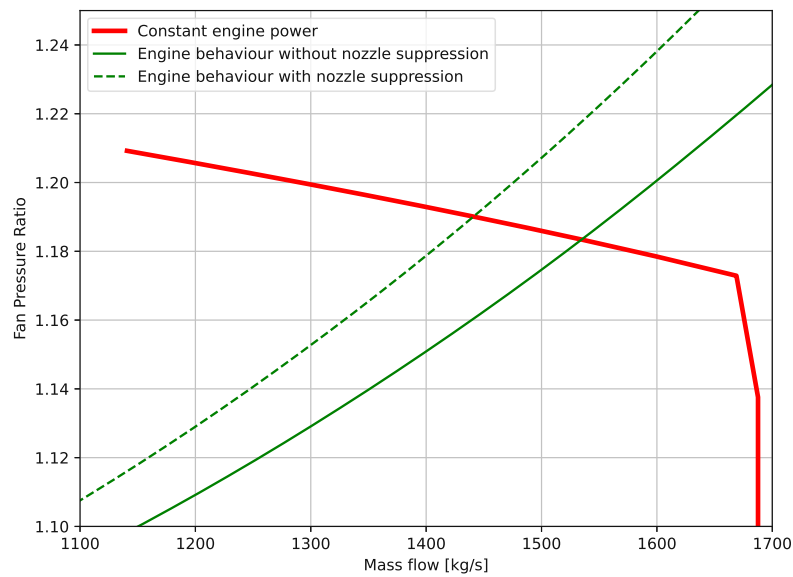


Figure 2.4: Engine operation curve for an engine with nozzle flow suppression and without nozzle flow suppression on a generic high bypass ratio engine

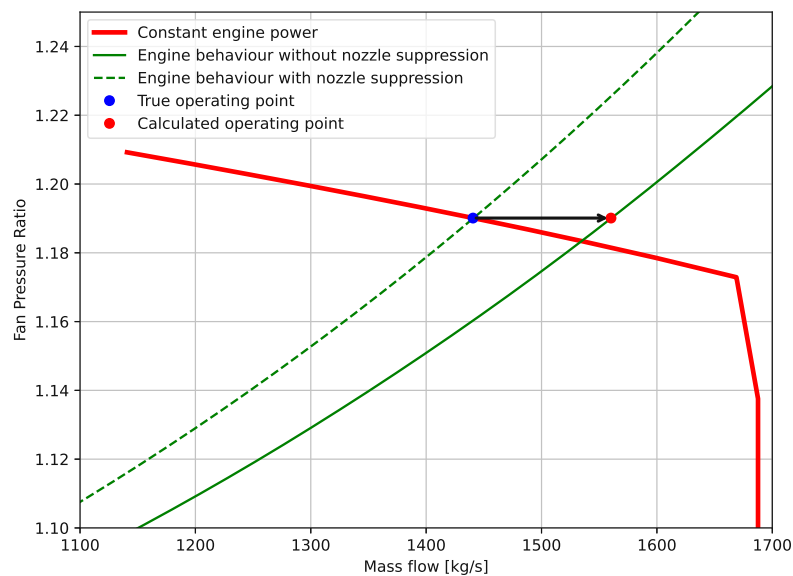


Figure 2.5: Thrust-drag book keeping error demonstrated on a generic high bypass ratio engine

## 2.5.2 Nozzle suppression coefficient

In order to correct for this inaccuracy, there are two methods. One would be to modify the measurement strategy in order to capture the mass flow directly instead of relying on assumptions concerning the nozzle exit pressure. This is discussed in further detail in Section 4.4. The other way is to correct for the mass flow delta by introducing additional terms into the book keeping model. This approach also helps to capture the error introduced by the standard book keeping approach. Noting equation 2.41, the actual mass flow can be related to the ideal mass flow by the nozzle suppression flow coefficient  $\Delta C_{D,supp}$ :

$$W_{17} = (C_D + \Delta C_{D,supp}) \cdot W_{17,id} \quad (2.46)$$

From equation 2.39, it is clear that the mass flow error arises from  $FNPR = \frac{P_{t17}}{P_{s0}}$  being incorrect. As the total pressure, total temperature and cross section remain constant, assuming  $C_D = 1$ ,  $\Delta C_{D,supp}$  can be computed as:

$$\Delta C_{D,supp} = \frac{W_{PR}}{W_{FNPR}} - 1 \quad (2.47)$$

As a result,  $\Delta C_{D,supp}$  is dependent on both the FNPR, as well as the static pressure coefficient at the nozzle exit. This can be seen in Figure 2.6.

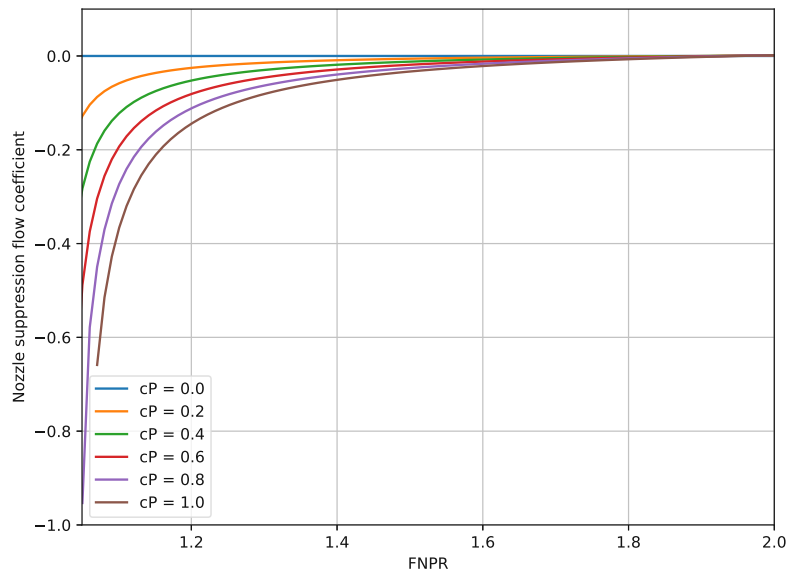


Figure 2.6: Nozzle suppression flow coefficients for various nozzle exit static pressure coefficients and FNPRs

Figure 2.6 shows that suppression effects are most pronounced at low FNPRs, reaching values below -0.2 for even moderate pressure coefficients. At higher FNPRs, the effect becomes significantly smaller, albeit still existent. Thus, it becomes clear that low pressure ratio engines are more strongly affected by nozzle suppression effects than high pressure ratio engines.

## 3 CFD methodology

The nacelle exit static pressure, as previously described, is responsible for the systematic errors in the drag-thrust bookkeeping approach. Therefore, in order to quantify this effect in more representative situations, the pressure field around an aircraft has to be determined. This can be performed via either experimental wind tunnel testing or using computational analysis. For the purposes of this research, the latter approach was chosen.

### 3.1 Geometry

#### 3.1.1 Common Research Model

The Common Research Model (CRM) was conceived in 2007, with its aerodynamic design finalized in 2008. Its aim was to promote cooperative research and development across multiple international institutions for the aim of improving computational and experimental aerodynamic research [13]. The goal was to create a representative geometry of a modern transonic transport aircraft, flying at a cruise Mach number of  $Ma = 0.85$  with a nominal lift condition of  $c_L = 0.50$  at a Reynolds number of  $R_n = 4.0 \cdot 10^7$ . NASA led the initial design, with a technical focus group (TFG) from Boeing completing the detailed aerodynamics [14].

This version of the CRM was designed around the cruise condition, hence the name Common Research Model - High Speed (CRM-HS). However, noting that low speed behaviour where high lift devices are deployed requires a different geometry, in 2018, Lacy et al. developed a High-Lift variant of the CRM, dubbed CRM-HL. This version added inboard and outboard leading edge slats, as well as inboard and outboard single slotted flaps [15]. The CRM-HL model geometry differs only in the definition of the wings, where, aside from the addition of the high-lift devices, the leading edge of the clean wing has been straightened in order to simplify the definition of the leading edge slat, as can be seen in figure 3.1.

Two versions of the model are available: a landing configuration, and a take-off configuration. The models differ by the deflection angles of both the slats and flaps -  $22^\circ$  and  $30^\circ$  for the slats, as well as  $25^\circ$  and  $37^\circ$  for the flaps of the take-off and landing configuration respectively [16].

The CRM-HL has been subject to multiple wind-tunnel tests, with two notable tests having taken place at the NASA QinetiQ 5-metre low speed wind tunnel in 2019 [17] and at the ONERA F1 wind tunnel in 2022 [18].

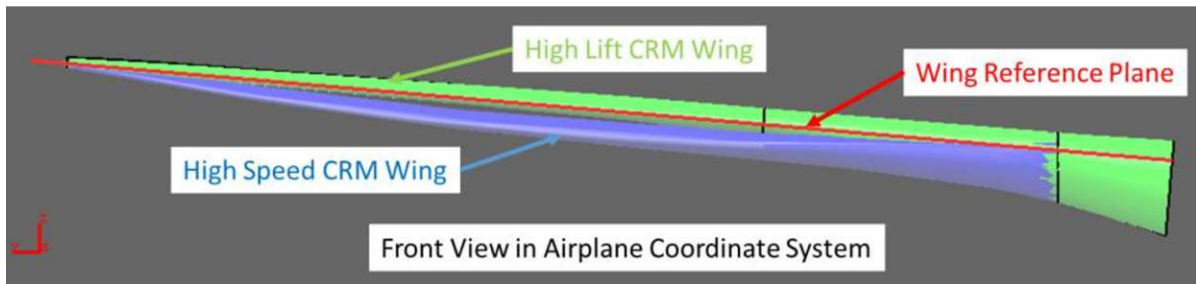


Figure 3.1: Leading edge modifications made to CRM-HL vs. CRM-HS (Source: [16])

### 3.1.2 CFD Model Geometry

In the base formulation of the CRM-HL geometry, each flap and slat is modelled as its own body compared to the main frame. This was done deliberately in order to improve the pre-processing workflow in CFD [15]. However, during wind tunnel testing, structural support is needed for all elements. Additionally, the presence of slat brackets and flap track fairings has an impact on the aerodynamic behaviour of the aircraft. Therefore, the wind tunnel models apply geometric modifications to the base model.

For the purposes of this research, the geometry selected is based heavily on the one used in the ONERA F1 wind tunnel test. The ONERA F1 wind tunnel model is derived from a 5.2% model of the CRM-HL, keeping most aerodynamic features of the wing, engine nacelle and fuselage identical. The major modifications include the inclusion of slat brackets and flap track fairings. Additionally, some further local thickness changes were introduced to facilitate model manufacturing [18]. These changes can be seen in figures 3.2 and 3.3.

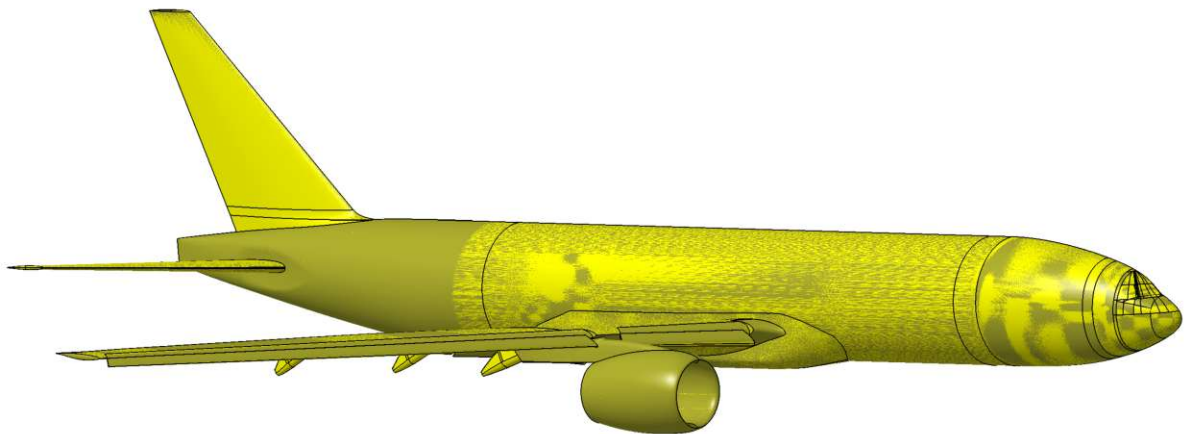


Figure 3.2: Geometry comparison of ONERA F1 model (yellow) against standard CRM-HL model (grey)

The wind tunnel model geometry poses some challenges for CFD analysis. The large number of slat brackets along, with their large number of sharp edges posing a difficult

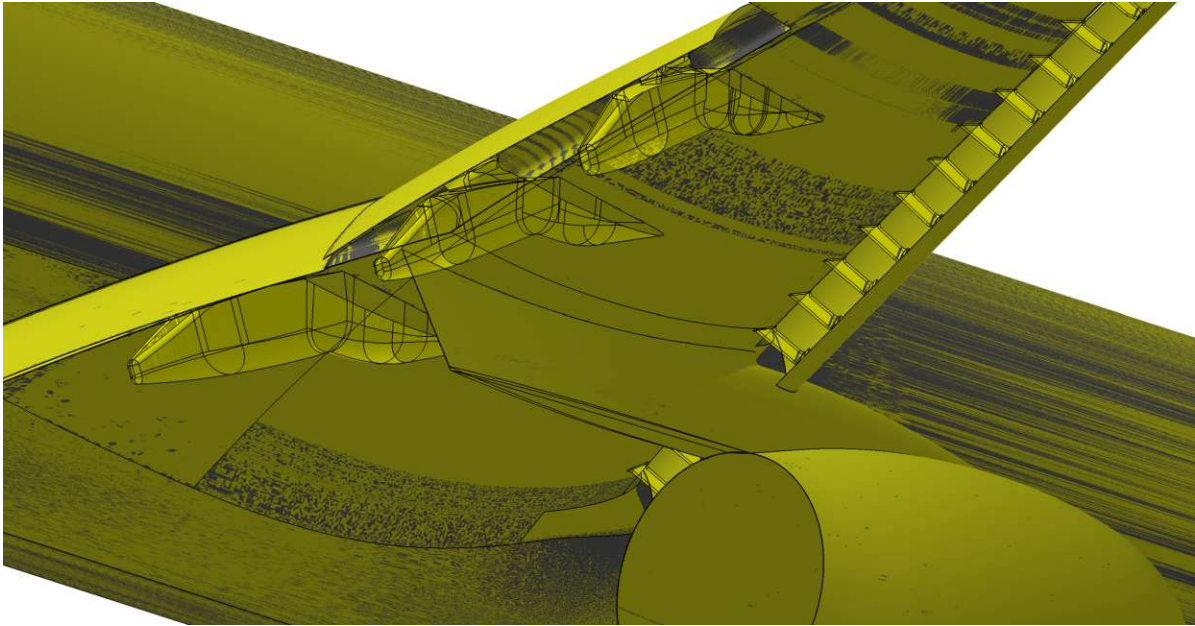


Figure 3.3: Detailed view of flap track fairings and slat brackets

scenario for the grid and solver to calculate accurately [19]. These issues can cause serious issues in achieving a convergent numerical solution. A possible solution is either the full removal of the slat brackets, or the removal of the mounting geometry [20]. This, however can lead to correlation issues as the separations off the slat brackets lead to pronounced "pizza slice" separation along the outboard part of the wing at high angles of attack [21]. As a consequence, the inboard slat brackets were removed, with the outboard slat brackets being simplified and having their mounting geometry removed, as seen in figures 3.4 and 3.5.

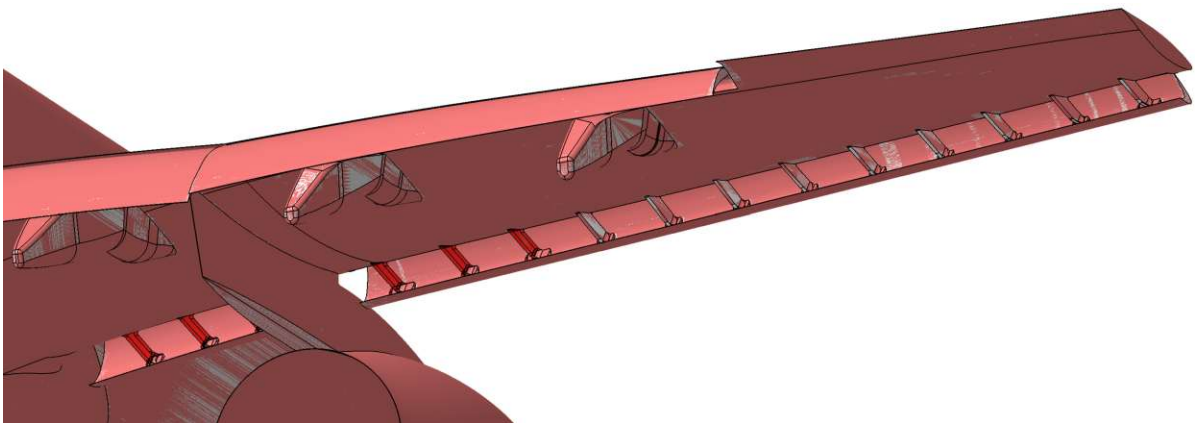


Figure 3.4: Changes from ONERA F1 geometry to final CFD geometry

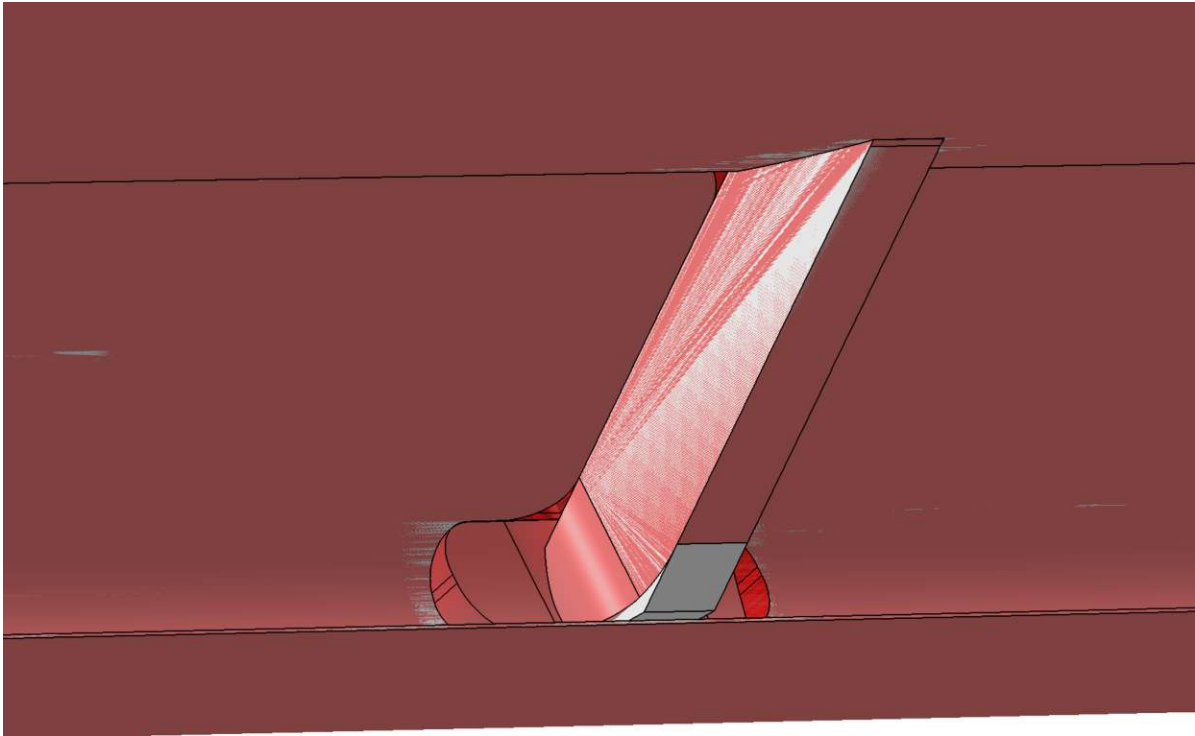


Figure 3.5: Detailed view of outboard slat bracket simplifications

### 3.1.3 TPS model geometry

The geometry is based on the TPS model by [22]. It features a twin-stream turbofan layout with a central exit cone. The inlet cone was removed, as the numerical conditions negate the need for one.

In order to install the engine on the frame, the empty flow-through nacelle of the CRM-HL was used as a positioning reference; thus, the toe-in angle of around 2.8 degrees was retained. The orientation of the engine relative to the aircraft was kept identical to the CRM engine. The TPS model features an increased outer diameter of the nacelle, which puts it fairly close to the inboard slats. Thus, in order to increase clearance and minimize flow interference with the high-lift devices, its axis was lowered by 250 mm relative to the CRM base engine.

The engine is mounted using a single pylon without bifurcation onto the wing. Its shape and alignment match the base CRM pylon closely, minimizing the potential for misalignment issues.

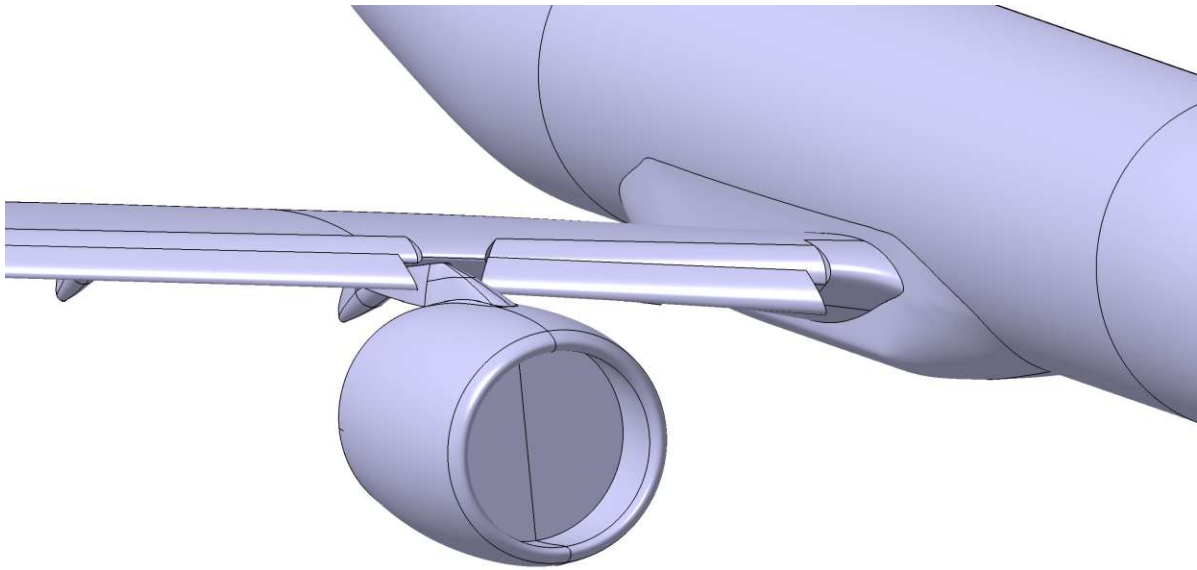


Figure 3.6: Mounted TPS on CRM-HL

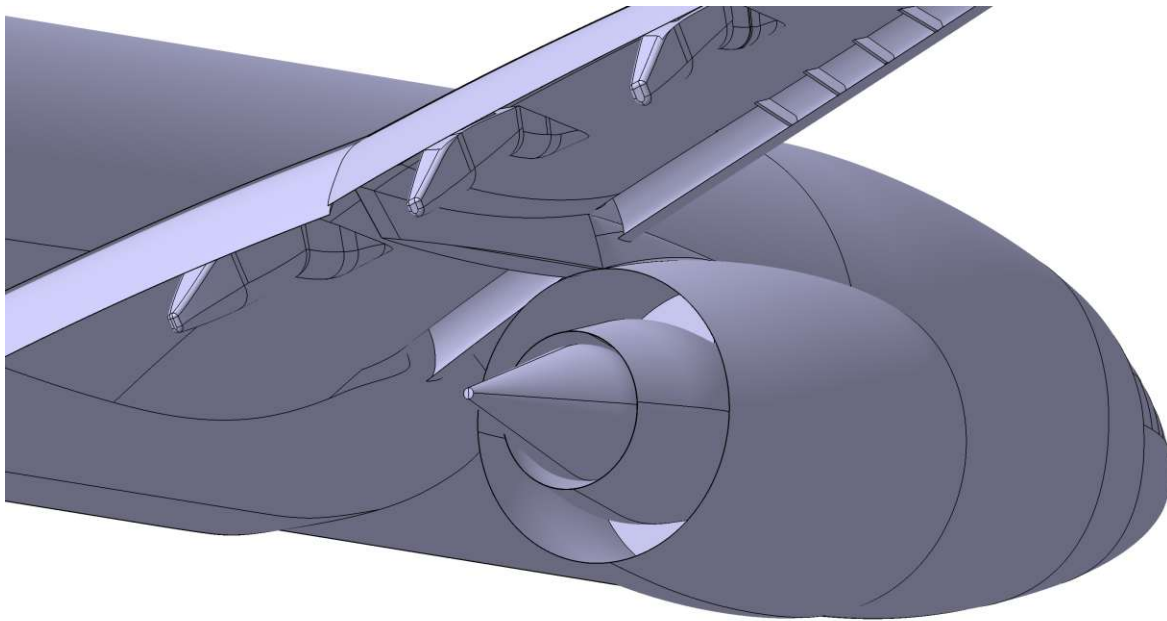


Figure 3.7: Detail view of TPS on CRM-HL

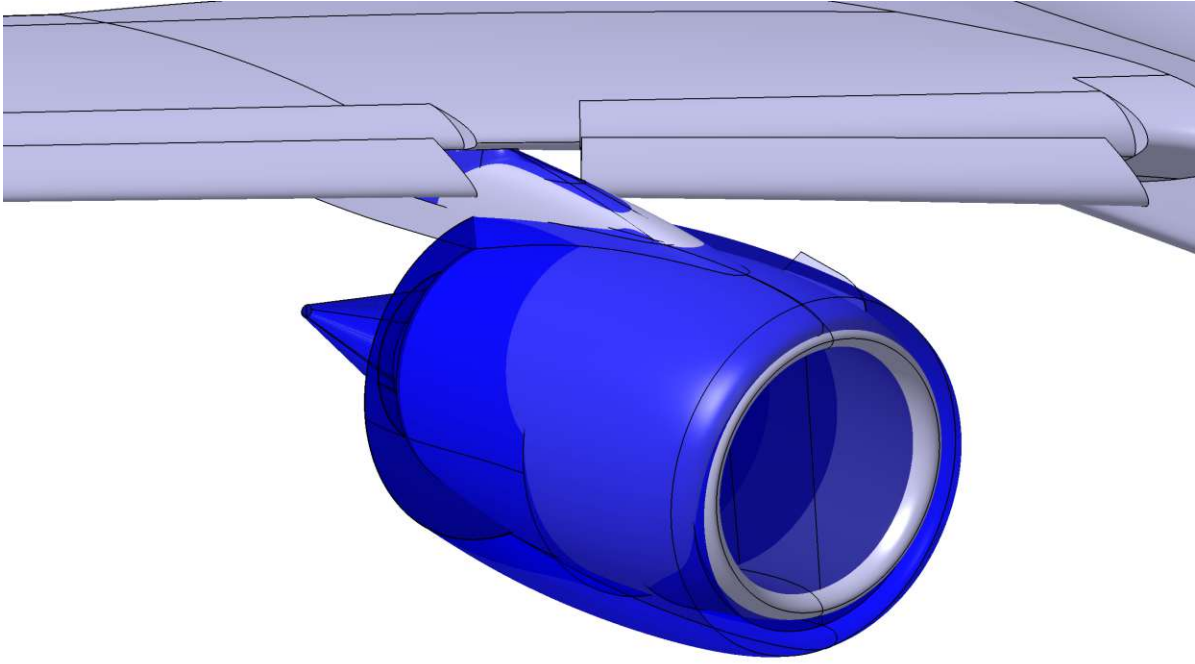


Figure 3.8: Comparison of TFN geometry to TPS geometry

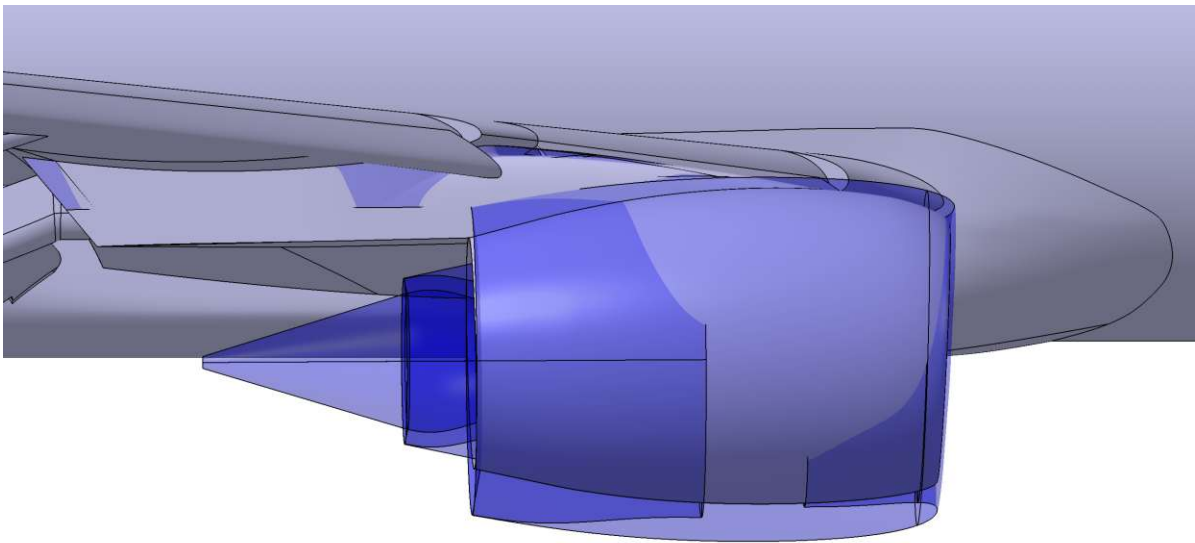


Figure 3.9: Comparison of TFN geometry to TPS geometry from side view

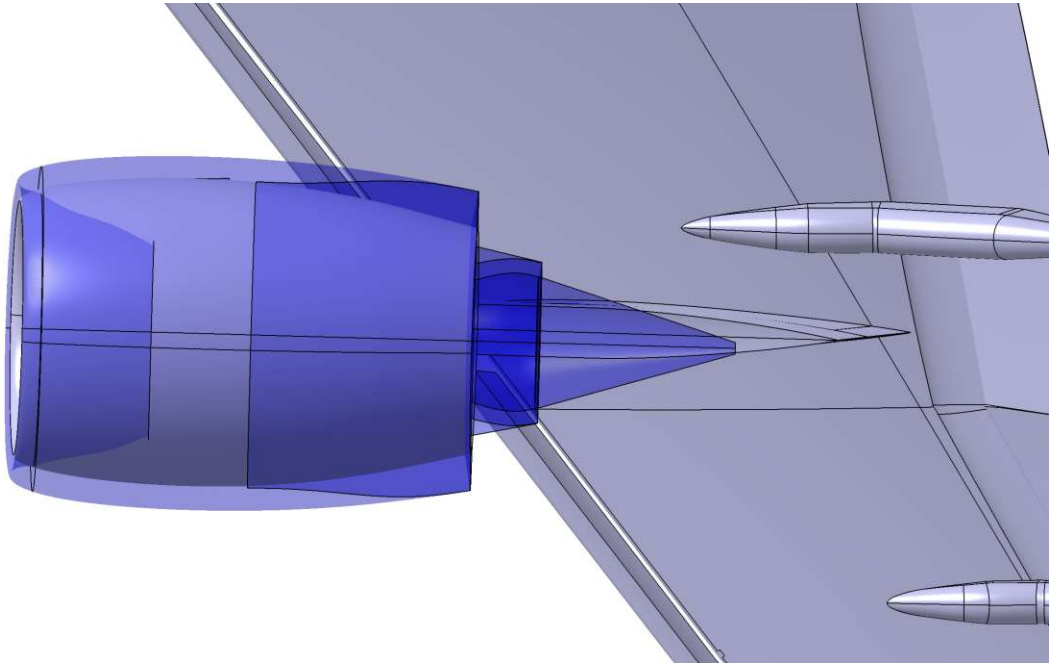


Figure 3.10: Comparison of TFN geometry to TPS geometry from bottom view

## 3.2 General parameters

In order to assess the pressure field at the exit duct of the nacelle, the external aerodynamic flow around the CRM-HL model has to be calculated. This is done by using Computational Fluid Dynamics (CFD). For the purposes of this thesis, the software StarCCM+ by Siemens was used.

### 3.2.1 Domain

The general setup of the model follows learnings established during the High Lift Prediction Workshop (HLPW) series. This involves a spherical computational domain with the aircraft positioned in the centre, and an external diameter of  $d = 200 \cdot C_{Ref}$  with the reference aerodynamic chord  $C_{Ref} = 7.005m$  [23]. In order to reduce computational cost, a semi-span model is used with symmetry conditions along the  $z$ - $x$  plane, mandating all gradients normal to the plane to be equal to zero.

### 3.2.2 Solvers

The physics are computed using a RANS model with Finite-Volume discretization. In order to capture potential compressible effects, ideal gas behaviour was modelled. Gradients were computed using a Roe FDS scheme with 1st order upwind interpolation scheme. The choice of a 1st order solver instead of a higher order scheme was in response to stability issues during initial stages of research. The mass and momentum conservation equations were solved using a density based coupled solver with automatic CFL control, limiting the maximum to 200 in order to prevent the solver from causing further instabilities.

In order to resolve the closure problem of RANS equations, a turbulence model has to be selected. The main contenders for use in external aerodynamics are the Spalart-Allmaras (SA) model and the  $k-\omega SST$  model. The  $k-\omega$  turbulence model was chosen, as it has shown in previous works to provide the best correlation to wind tunnel data compared with other turbulence models [21]. Following recommendations from [21], the Realizability coefficient was changed from its default value of 0.6 to 1.2. Similarly, the  $a_1$  value was changed from 0.31 to 1.0.

Farfield turbulence was specified using a combination of  $k$  and  $\omega$  values. The calculation follows the best practice recommendations of Siemens [24]. The turbulence kinetic energy  $k$  is computed as:

$$k = (1.0 \cdot 10^{-6}) \cdot U_{\infty}^2 = 0.011m^2/s^2 \quad (3.1)$$

The specific dissipation rate  $\omega$  is computed as:

$$\omega = 5.0 \cdot \frac{U_\infty}{L_c} = 73.448s^{-1} \quad (3.2)$$

where  $L_C = C_{ref}$ .

Convergence was assessed by applying a combined asymptotic condition onto the lift coefficient and drag coefficient of the aircraft, as well as onto the average pressure on the exit plane of the engine nacelle. A target of 0.3% maximum deviation over 250 iterations was chosen, with a lower limit of 500 iterations and an upper limit of 5000 iterations to prevent both false convergence during early stages of the run, as well as excessive run time for periodic fluctuations in the final solution.

### 3.3 TPS model

The inclusion of a TPS in the CFD model requires some adaptations. While the domain and the main aircraft geometry remain identical, the presence of the TPS changes the boundary conditions around the engine.

The general setup follows the work by Rudnik et al. [25], who proposed the modelling of a TPS using a mass flow outlet for the fan entry face, as well as stagnation inlets for the fan and core outlet faces. The fan inlet face features a mass flow outlet condition, while the core and fan outlet faces each feature a mass flow inlet. As such, this is not a true TPS where pressurised air is used to drive the airflow; instead, this more closely emulates a turbofan engine. The setup of the boundary conditions can be seen in Figure 3.11.

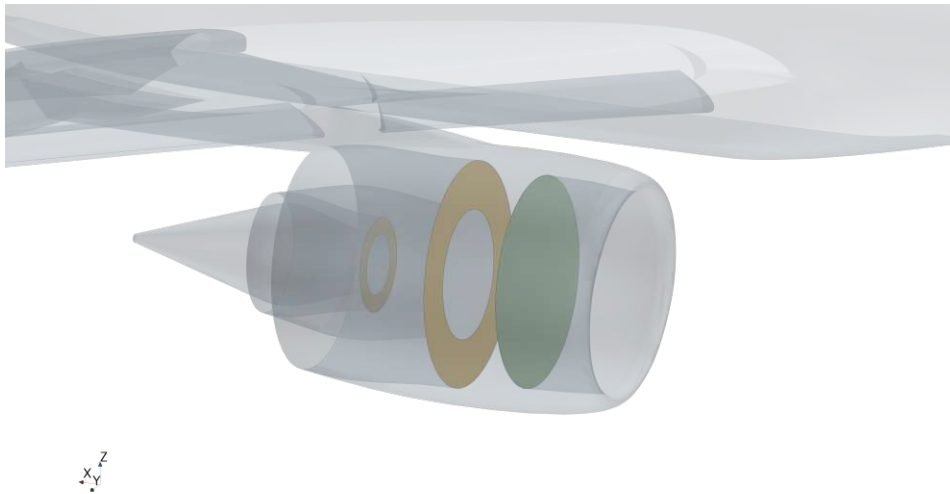


Figure 3.11: Boundary condition regions for the TPS model (Yellow: Inlets, Green: Outlet)

As highlighted in [26], the use of this method requires prescription of several boundary conditions. The fan inlet face boundary condition is set by specifying the mass flow rate, which is the sum of both core and fan mass flow. The pressure condition is extrapolated from the core mesh. The fan and core outlet planes require additional values in order to close the system. In addition to the mass flows, the total temperature needs to be specified as well. In case of supersonic flow, the static pressure also needs to be specified, as the lack of information transfer upstream for supersonic flows makes extrapolation from the core mesh impossible.

In order to calculate the boundary conditions, a model developed by the TU Wien was used [22]. This model is a 0-D model which follows the engine station convention from [12]. The modelled TPS is a generic Ultra High Bypass Ratio (UHBPR) turbofan with a design fan pressure ratio (FPR) of 1.3. The thrust is set by varying the FPR in steps from 1.1 to 1.5. The resulting mass flows and total temperatures can be seen in Table 3.1.

FPR	$W_5$ [kg/s]	$W_{15}$ [kg/s]	$T_{t5}$ [K]	$T_{t15}$ [K]
1.1	105.47	1089.8	208.14	302.67
1.2	169.26	1268.1	178.13	299.08
1.3	213.98	1371.5	171.62	319.58
1.4	236.22	1435.3	167.06	327.45
1.5	238.37	1473.5	166.64	334.90

Table 3.1: TPS boundary conditions for different thrust ratings

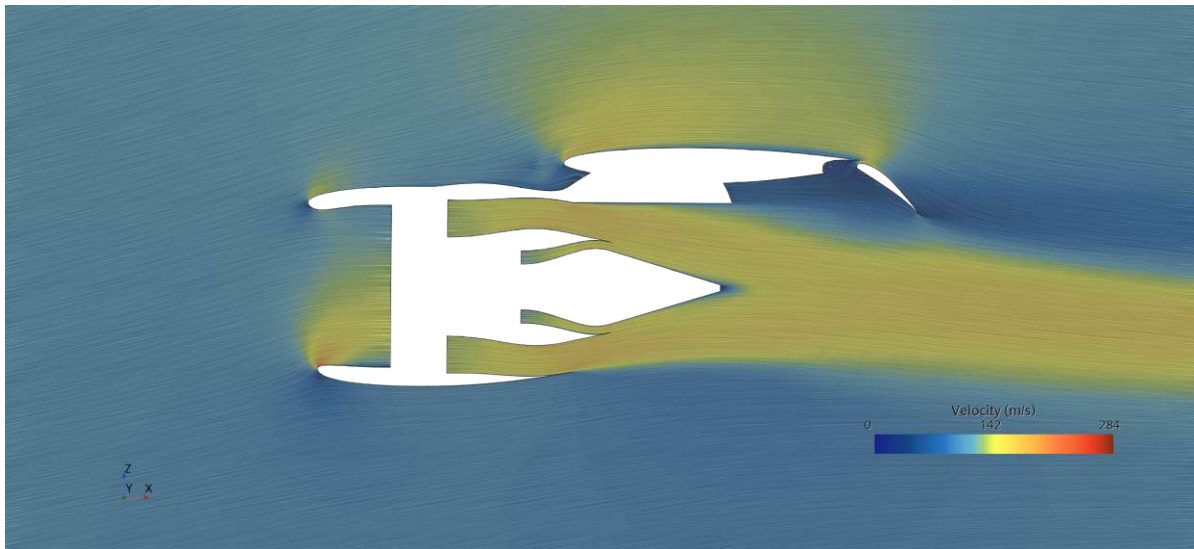


Figure 3.12: Velocity field around the TPS engine at  $\alpha = 10deg$  and  $FPR = 1.3$

## 3.4 Mesh

### 3.4.1 General setup

The general setup is based around a polyhedral core mesh with an enhanced quality triangle surface mesh and prism layer meshing for near-wall regions. As near-wall behaviour is crucial, a fully resolved boundary layer approach was chosen, which dictates a  $y^+$  value of around 1, and no higher than 4.

The polyhedral core mesh is designed to be fairly coarse in the farfield domain, with local refinements on both the surface, particularly on the wings and slat brackets, as well as volume refinements, especially around the wing itself, the wing tip vortex, the wing-fuselage junction, the engine outlet, as well as general wake refinements, as seen in Figure 3.13.

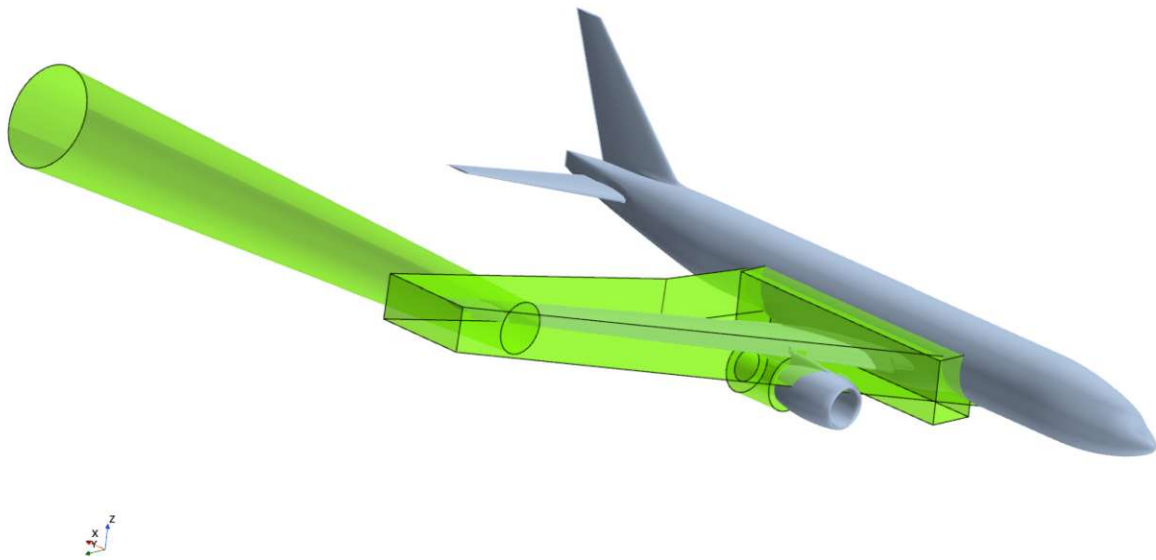


Figure 3.13: Refinement volumes

To capture the boundary layer, prism layers are employed in the near-wall domain. As the target  $y^+$  value requires a first-cell spacing of  $y = 0.005mm$ , a total of 38 prism layers are used in order to prevent excessively high volume ratios, improving the numerical response. The overall thickness was based on flat plate boundary layer theory, with some added thickness along the top of the wing in order to capture the slat wake. With the thickness specified, the growth ratio was calculated automatically. The aim was achieved, as seen in Figure 3.14.

Due to the blunt geometry of the trailing edges, driven by manufacturing concerns [18], the local resolution is critical. The importance arises from both local losses requiring



Figure 3.14: Wall  $y^+$  values for the first cell

a suitable amount of resolution, as well as the sharp angle towards the adjacent surfaces creating heavily skewed cells with poor aspect ratios. In order to ensure adequate representation of the trailing edge geometry, a minimum of 3 cells per TE thickness was prescribed. This ensures that the mesh does not collapse towards the trailing edge. An increased number of TE cells would significantly increase the cell count, therefore, following learnings from [21], it was kept at 3. This can be seen in Figure 3.15.

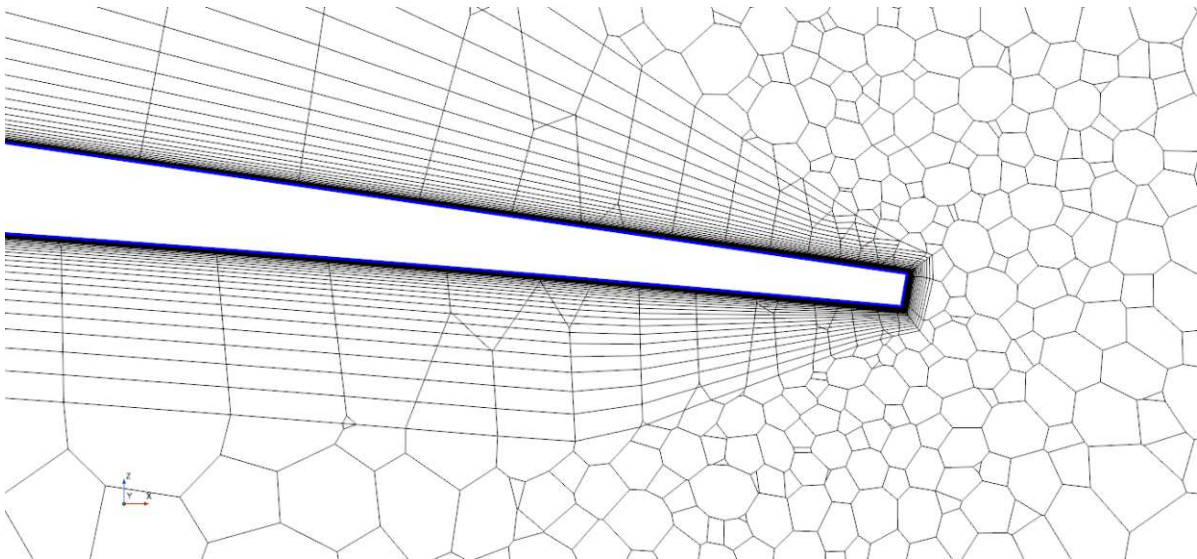


Figure 3.15: Mesh slice at the trailing edge

For the purpose of improving the flow prediction around stagnation points, a minimum of 48 points per circle was specified. This, along with a surface growth rate of 1.2 and a volume growth rate of 1.15 results in low cell volume ratios and improved resolution around areas with high local curvature and thus strong gradients.

The parasolid modeller of StarCCM+ is not capable of handling geometries larger than 1000 m, which is not sufficient to capture the domain size. To circumvent this, the polyhedral mesh was created for a domain with diameter  $d_{poly} = 998m$ , followed by extruding the surface mesh of the outer boundary until the domain size requirement was fulfilled. This is shown in Figure 3.16.

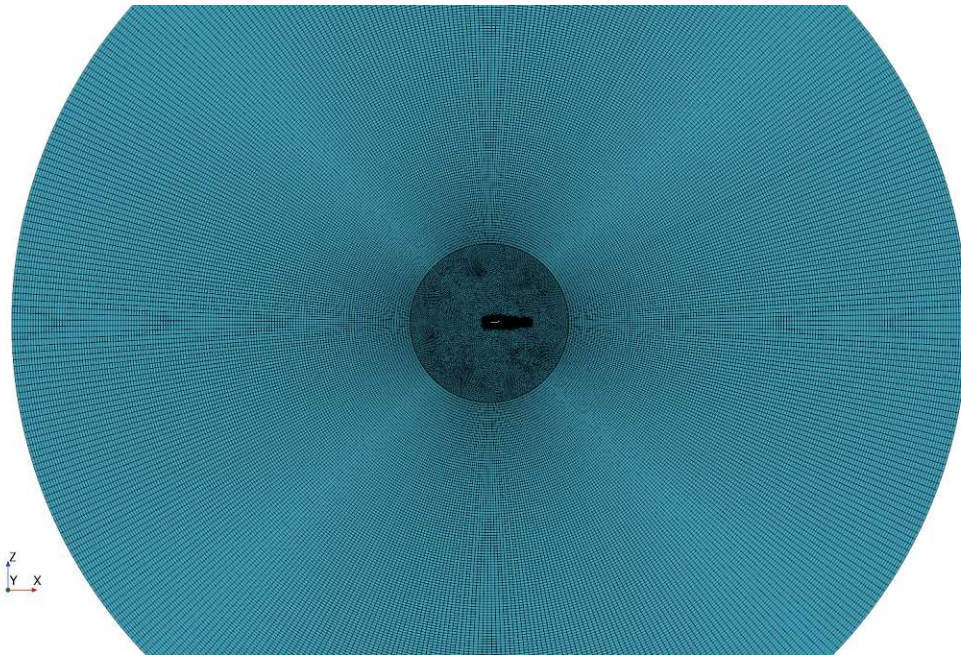


Figure 3.16: Mesh slice at symmetry plane

### 3.4.2 Mesh independence study

Due to the numerical nature of the model, there is an inherent discretization error. This error needs to be minimized, which necessitates a Mesh independence study. For this, the base size of the mesh was based on the number of cells per the length of the reference chord. This allows for a single parameter to refine the mesh globally, thus providing a good parameter for mesh independence studies. As the  $y^+$  target is set by the freestream conditions, the prism layers were not altered between the different versions. Likewise, the number of cells along the trailing edge thickness was kept consistent. All analysis was performed at an angle of attack of 4 deg.

Figures 3.17 to 3.19 show the behaviour of lift coefficient, drag coefficient and average nacelle exit pressure coefficient over the cell count. The values are compared to

the equivalent configuration tested in the ONERA F1 wind tunnel test - including the installed engine configuration, deployed high lift devices

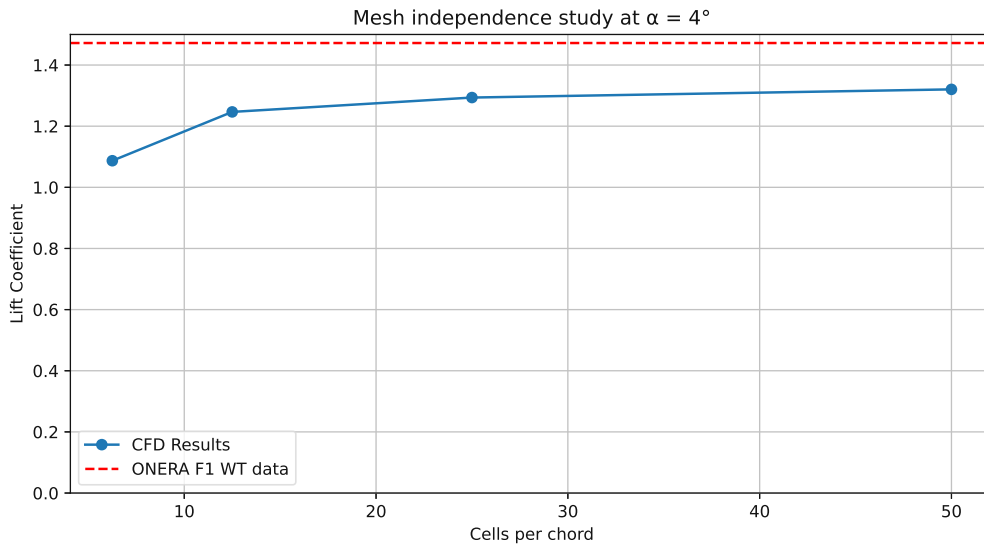


Figure 3.17: Lift Coefficient grid convergence study

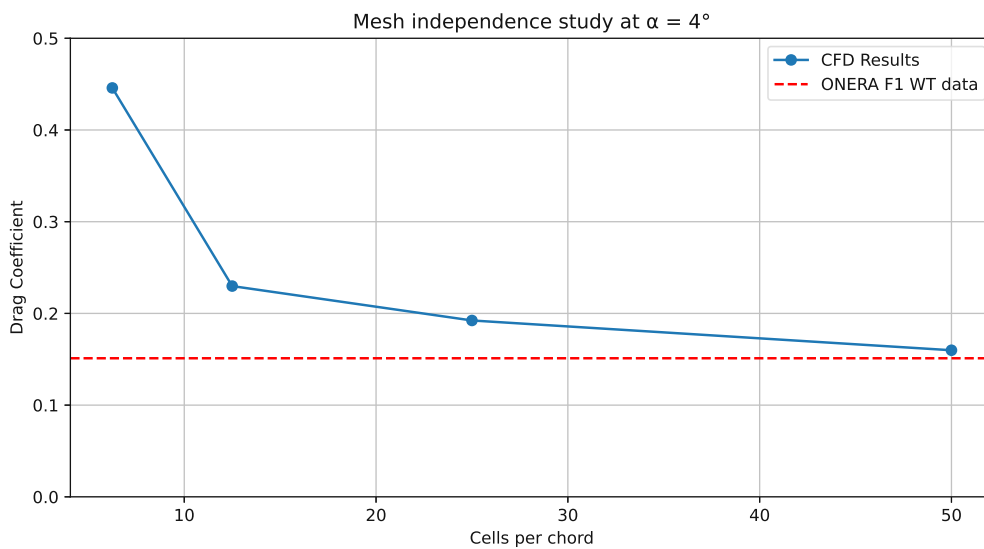


Figure 3.18: Drag Coefficient grid convergence study

It is visible that the lift coefficient does not match that of the wind tunnel test, even at higher grid resolutions. On the other hand, the drag coefficient appears to match the wind tunnel results well for higher resolution. Both plots show clear asymptotic behaviour.

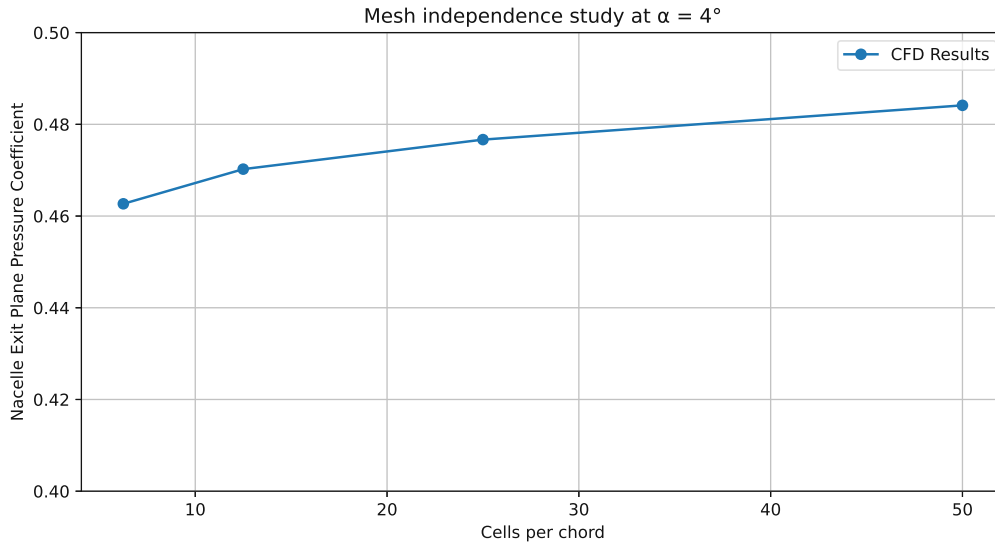


Figure 3.19: Average Pressure Coefficient at Nacelle Exit Plane grid convergence study

The average pressure coefficient at the nacelle exit plane shows limited change over the range of grid resolutions. As this value is of higher interest for this particular thesis, it can be assumed that the grid resolution is sufficient to capture the necessary flow phenomena.

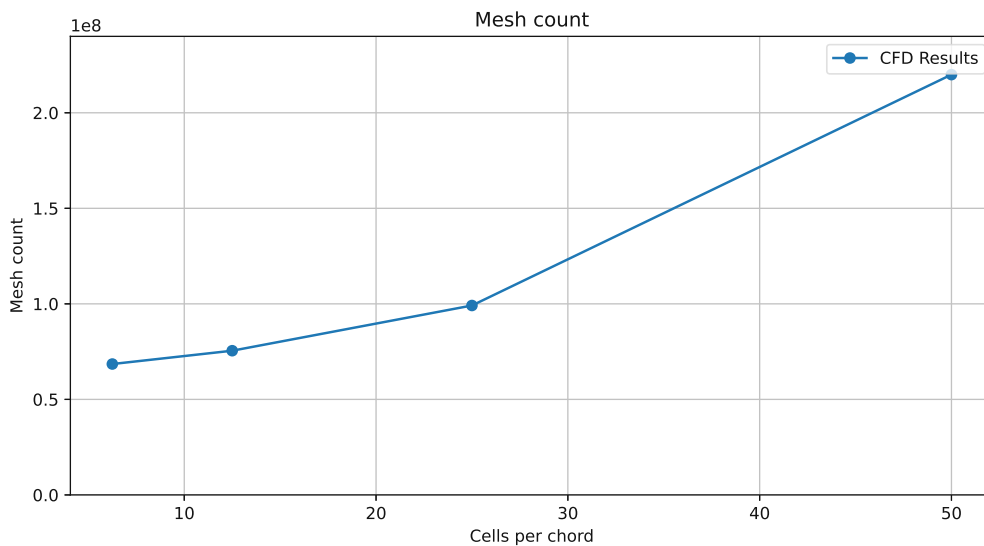


Figure 3.20: Cell count for Grid convergence study

Figure 3.20 shows the relationship of the total number of cells to the Cells per Chord value. At lower values, the trailing edge resolution and prism layers dominate the spa-

tial resolution, leading to only mild changes in cell count. At higher values, the spacial resolution of the off-body mesh leads to a large increase in cell count, which makes computation for CpC-values of above 50 very expensive and difficult from a computational standpoint. Thus, the choice was made to run all further simulations at CpC-values of 50. A visual overview of all tested grids is visible in Figures 3.21.

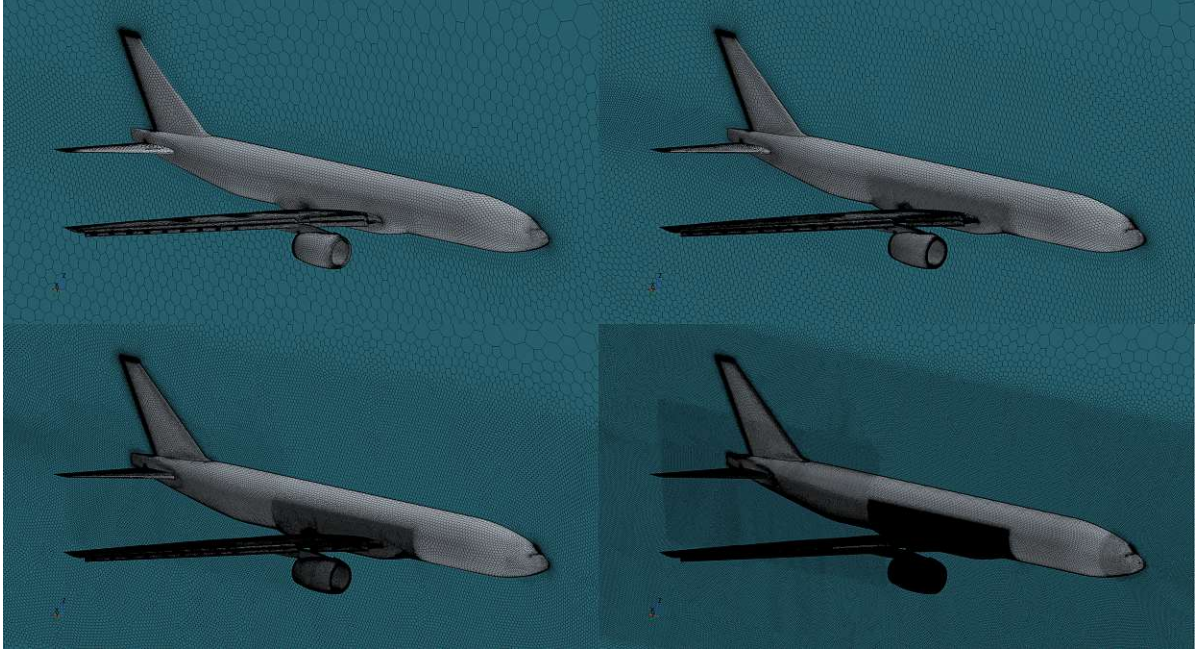


Figure 3.21: Grids for CpC values of 6.25 (top left), 12.5 (top right), 25 (bottom left), 50 (bottom right)

As the wings have the biggest impact on both aerodynamic coefficients, as well as the pressure field around the engine, achieving good local resolution is important. Figures 3.22 and 3.23 show the surface mesh on the finest resolution.

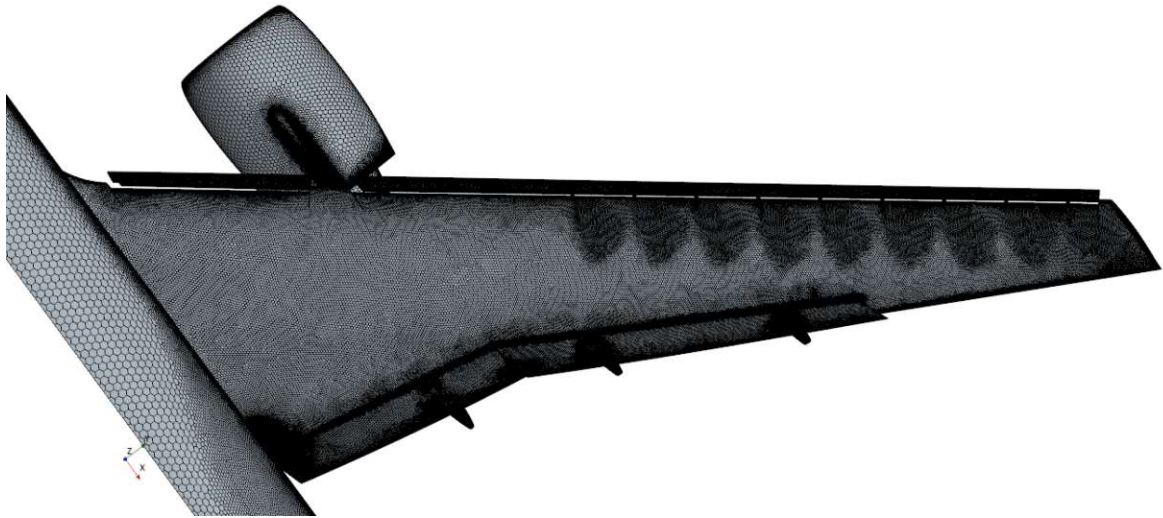


Figure 3.22: Wing top surface mesh for finest resolution

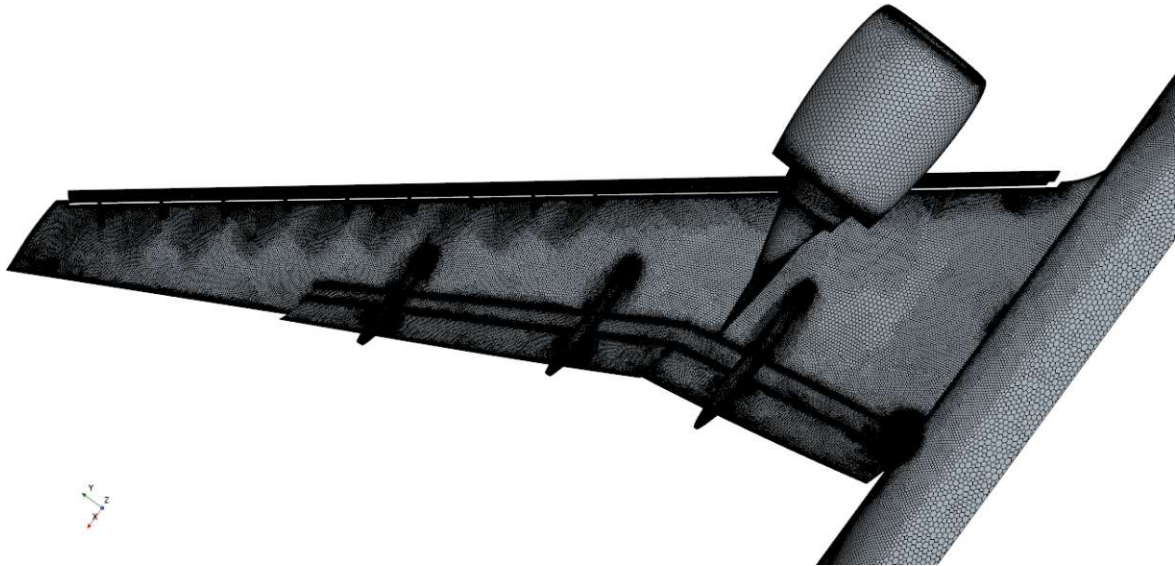


Figure 3.23: Wing bottom surface mesh for finest resolution

### 3.5 Model verification

In order to verify the accuracy of the model, it was solved for various angles of attack and compared with results from the ONERA F1 wind tunnel test [18]. Those results are shown in Figures 3.24 and 3.25:

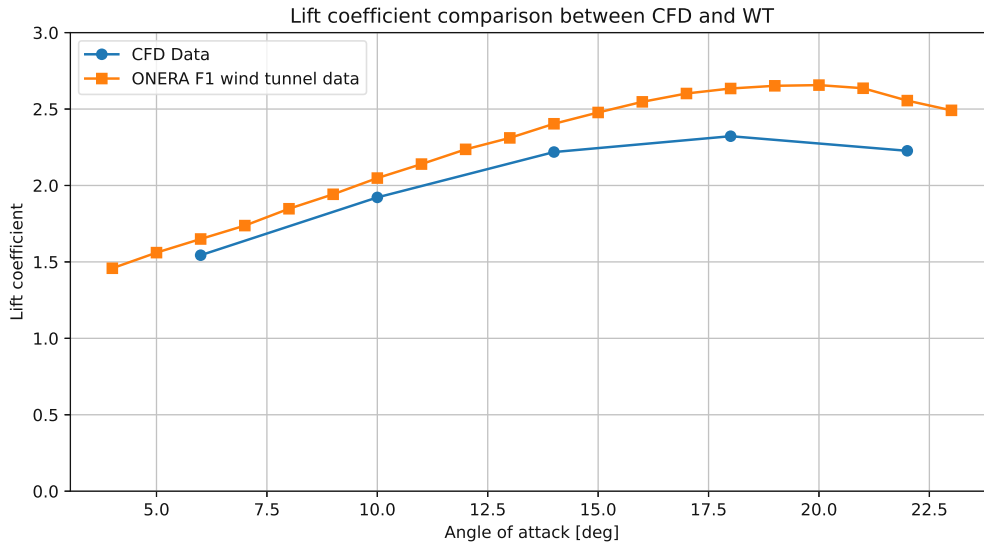


Figure 3.24: Comparison of lift coefficient between CFD and wind tunnel data

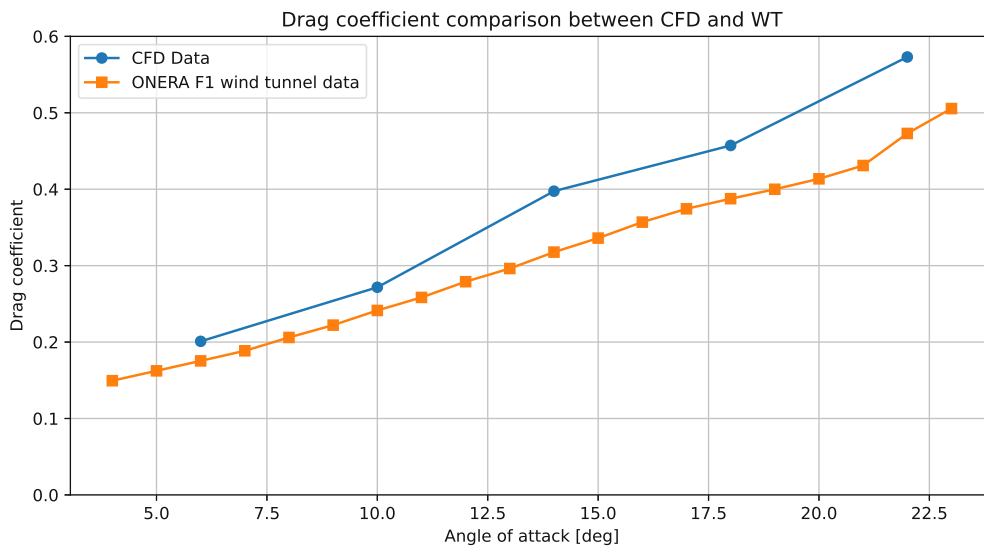


Figure 3.25: Comparison of drag coefficient between CFD and wind tunnel data

It is visible that there is a discrepancy between the CFD results and wind tunnel data. Particularly at higher angles of attack, the predicted lift coefficient is significantly lower than that measured in the wind tunnel experiment. This indicates worse flow attachment in CFD than in wind tunnel experiments, which is confirmed by previous work [23].

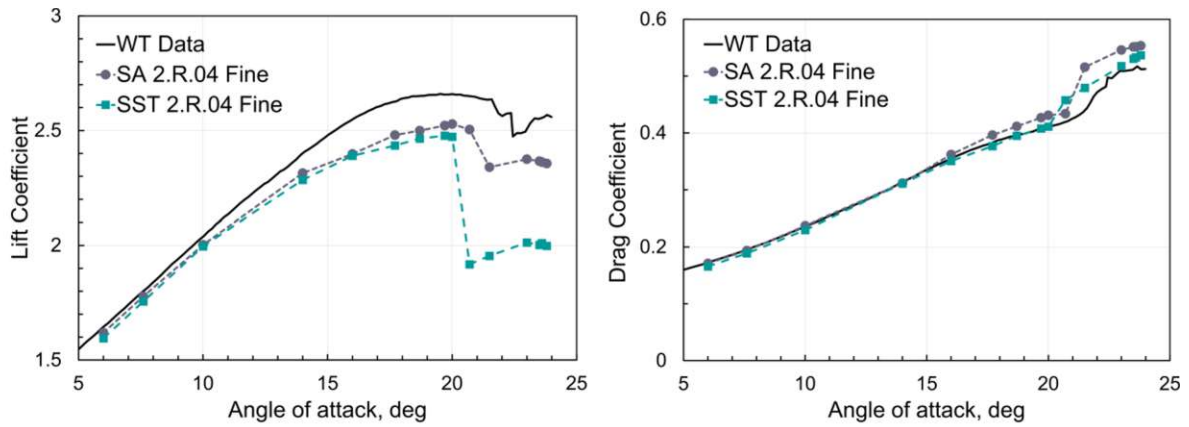


Figure 3.26: Results from Siemens [21] for lift and drag coefficients of the CRM-HL ONERA F1 wind tunnel test geometry in CFD

CFD results from [21] and [23] both show the difficulty of capturing accurate lift and drag coefficients at high AoAs. Figure 3.26 shows a similar trend with an initial offset during the linear range and a strong drop-off relative to the wind tunnel results at higher AoAs.

## 4 Suppression effect analysis

### 4.1 Impact of Angle of Attack for a TFN

At higher angles of attack, the lift of a wing increases until it experiences flow separations. This is due to an increase in lift force from both the low pressure surface on top, as well as the high pressure surface on the bottom of the wing. This increased pressure has the potential to increase the fan nozzle exit static pressure, leading to increased engine suppression effects.

In order to investigate this, the Through-Flow-Nacelle (TFN) model was run at a variety of angles of attack. The list of case run configurations can be seen in Table 4.1.

Case 1 - TFN AoA Sweep				
Case	Engine Geometry	HL Device Configuration	AoA	Mach number
1.1	TFN	LDG	6 deg	0.3
1.2	TFN	LDG	10 deg	0.3
1.3	TFN	LDG	14 deg	0.3
1.4	TFN	LDG	18 deg	0.3
1.5	TFN	LDG	22 deg	0.3

Table 4.1: CFD Simulation parameters for analysis of AoA impact on suppression effects on a TFN

Figure 4.1 shows a gradual increase of the static pressure in the outlet with increasing angle of attack, reaching its maximum at  $\alpha = 14 \text{ deg}$  AoA. After that, it gradually declines, which is an unexpected result. An investigation into the actual shape of the nacelle exit pressure distribution reveals a strong left-right trend, with increased pressure towards the inboard side, and lower pressure towards the outboard side. This can be seen in Table 4.2.

The source of the pressure asymmetry is caused by the external flow field around the aircraft at high angles of attack. The pressure field underneath the aircraft causes outwash, which increases the local AoA onto the side of the engine, as can be seen in Table 4.3. This materializes in the form of leading edge suction along the outside of the engine.

The majority of the pressure drop on the outboard side originates from airflow curvature. Due to the angle of attack of the aircraft, the external airflow no longer passes through the engine axially, but curves around it circumferentially. This causes an increase in pressure along the bottom of the engine, as well as a drop in pressure on the side of

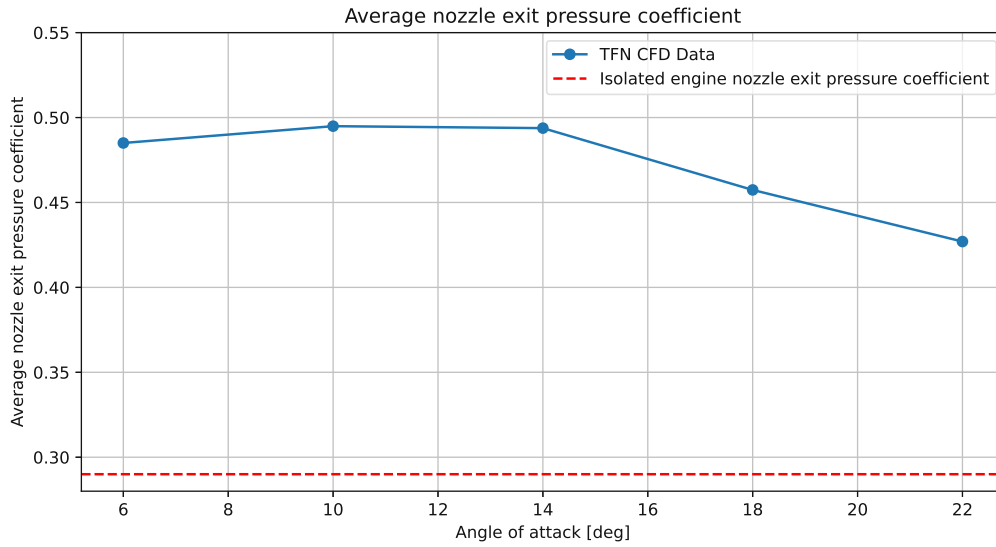


Figure 4.1: Area averaged nozzle exit pressure coefficient for an installed TFN engine (Case 1)

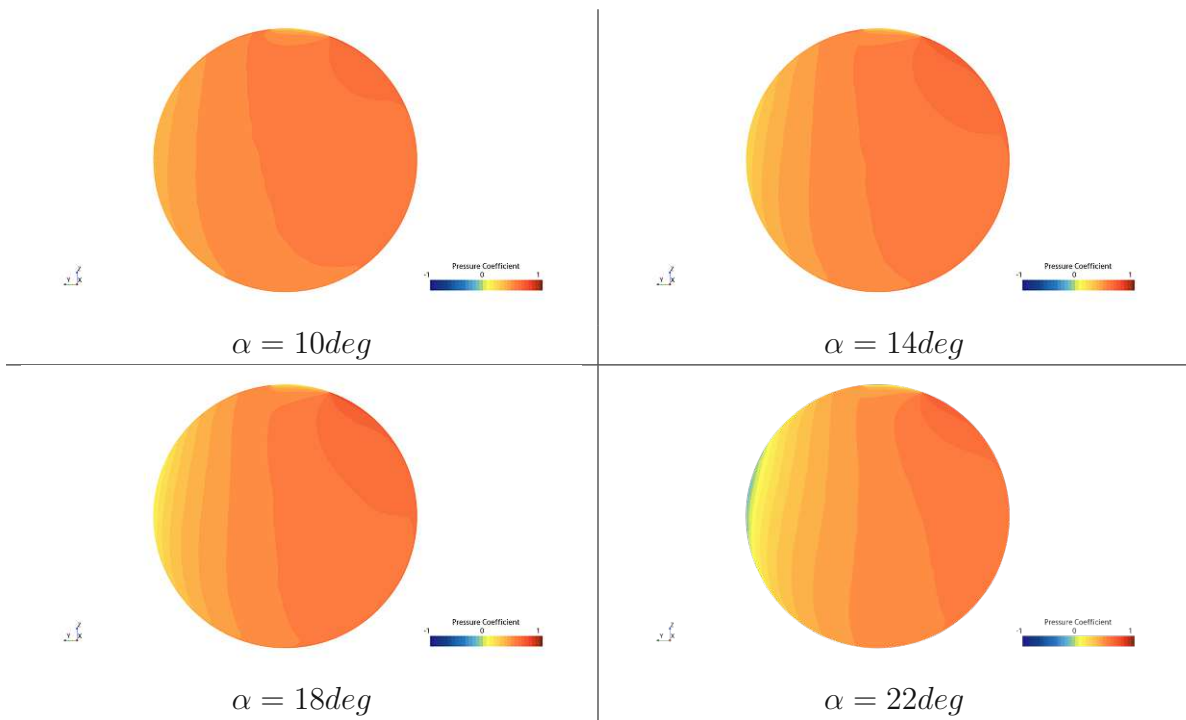


Table 4.2: Comparison of the installed nacelle exit pressure field at various angles of attack (Case 1)

the engine. This is supported by the presence of the lowest pressure spots being along the half-height of the engine, inclined at a slight angle. The asymmetry of this drop in

pressure is driven by the swept wing which blocks this curvature on the inboard side of the engine, but leaves the outboard side in freestream. This can be seen in Table 4.4.

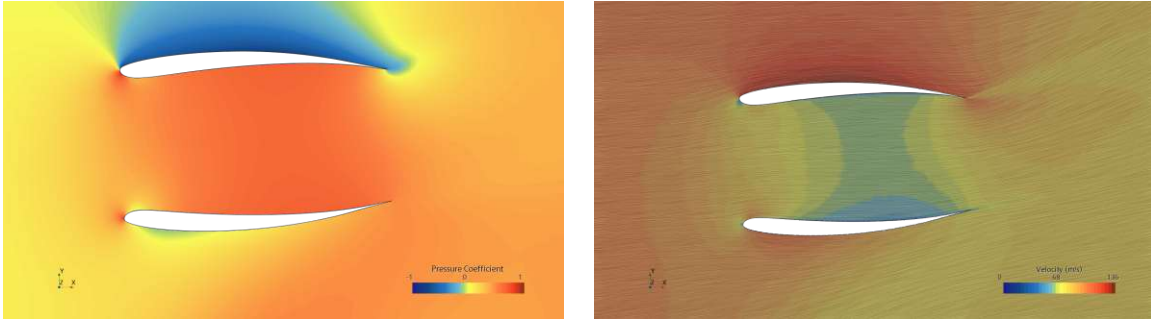


Table 4.3: Pressure coefficient (left) and velocity vector (right) field around the installed engine nacelle at  $\alpha = 22deg$  (Case 1.5)

Additionally, the impact of the wing interaction can be seen in Figure 4.1 as well. Berens et al. have shown the average pressure along the engine nacelle exit of the CRM to be around 0.41 for a Mach number of 0.7 [10]. Using the Prandtl-Glauert correction, the pressure coefficient at a freestream Mach number of 0.3 can be calculated. This value was further confirmed by CFD analysis.

$$C_{P|Ma=0.3} = C_{P|Ma=0.7} \cdot \frac{\sqrt{1 - 0.7^2}}{\sqrt{1 - 0.3^2}} = 0.307 \quad (4.1)$$

Comparing the measured values on the CRM-HL to the pressure values of the isolated engine, it is clear that wing induced suppression plays a major role, reaching  $c_P$  deviations as high as 0.2 for  $\alpha = 14deg$ . This shows that for the estimation of nozzle suppression flow coefficients, isolated testing is not sufficient.

Using the measured pressure coefficients,  $\Delta C_{D,supp}$  can now be computed. As the TFN does not have an active fan, the result is plotted over a variety of FNPR values to evaluate the impact for different engine designs. This is shown in Figure 4.2.

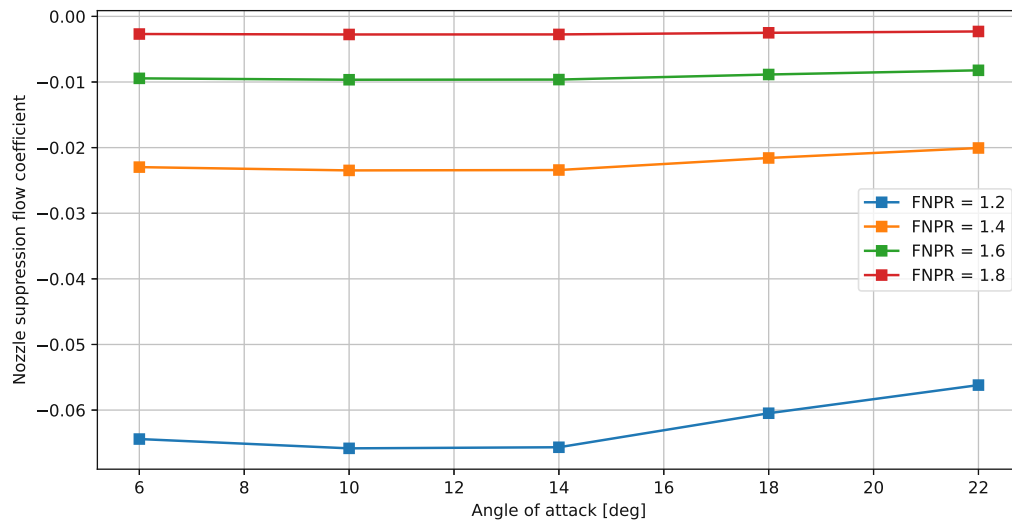


Figure 4.2: Nozzle suppression flow coefficients for a TFN engine (Case 1)

Once again, it can be clearly seen that the impact of flow suppression is most dominant at low FPRs and medium AoAs. For extremely low FNPRs, flow coefficients can reach values of -0.065, leading to severe errors in thrust, and by extension, drag prediction.

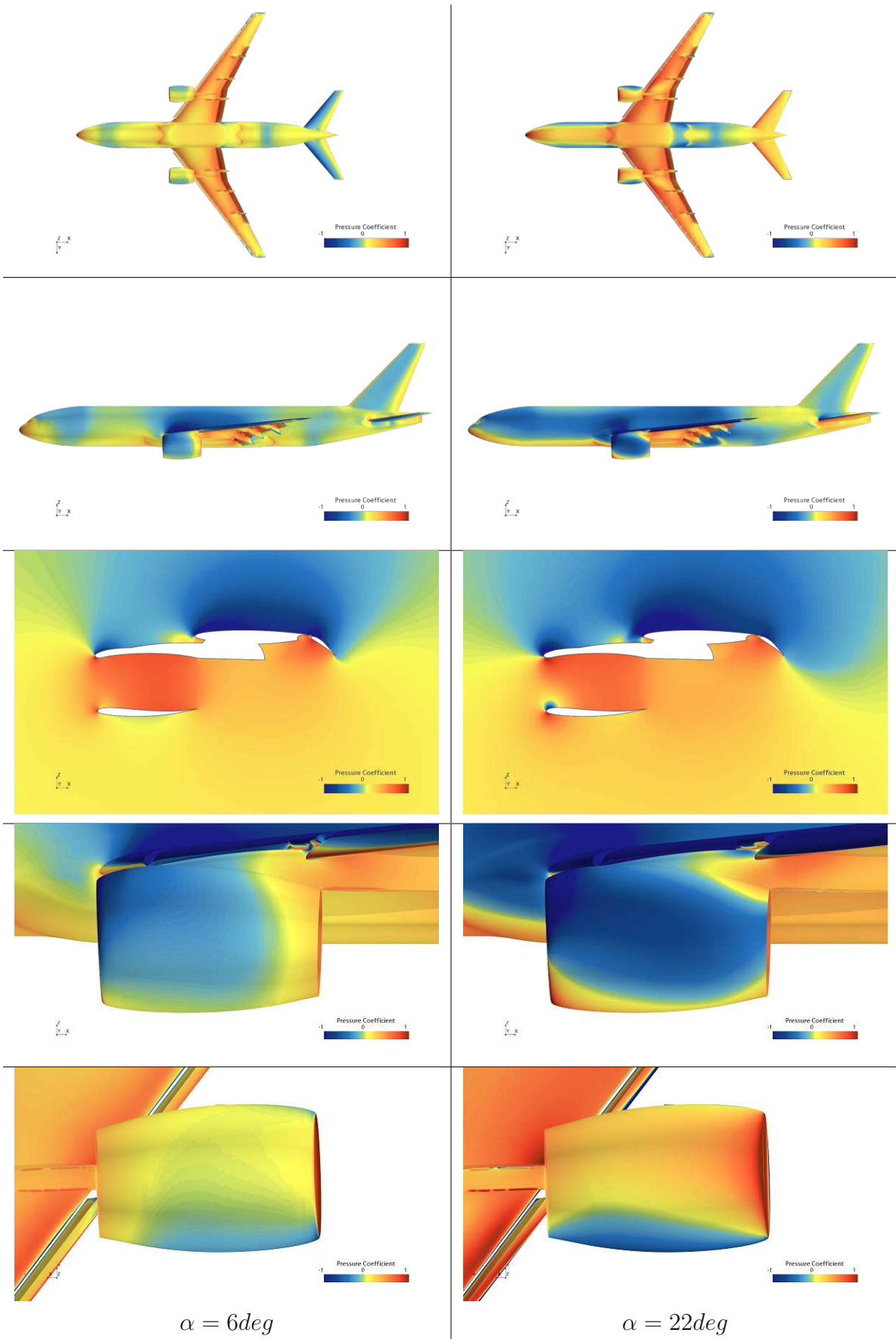


Table 4.4: Pressure field comparison for  $\alpha = 6deg$  and  $\alpha = 22deg$

## 4.2 Impact of Angle of Attack for a TPS

The interaction of the flow around the engine and the interference by the wing is driven to a large extent by the flow through the engine itself. A TPS increases the total pressure in the flow, thus creating thrust and affecting the flow field significantly. To assess this impact, the TPS model was run at an FPR of 1.3 across the same AoA range as in section 4.1. The list of case run configurations can be seen in Table 4.5.

Case 2 - TPS AoA Sweep					
Case	Engine Geometry	FPR	HL Device Configuration	AoA	Mach number
2.1	TPS	1.3	LDG	6 deg	0.3
2.2	TPS	1.3	LDG	10 deg	0.3
2.3	TPS	1.3	LDG	14 deg	0.3
2.4	TPS	1.3	LDG	18 deg	0.3
2.5	TPS	1.3	LDG	22 deg	0.3

Table 4.5: CFD Simulation parameters for analysis of AoA impact on suppression effects on a TPS

The results can be seen in Figure 4.3.

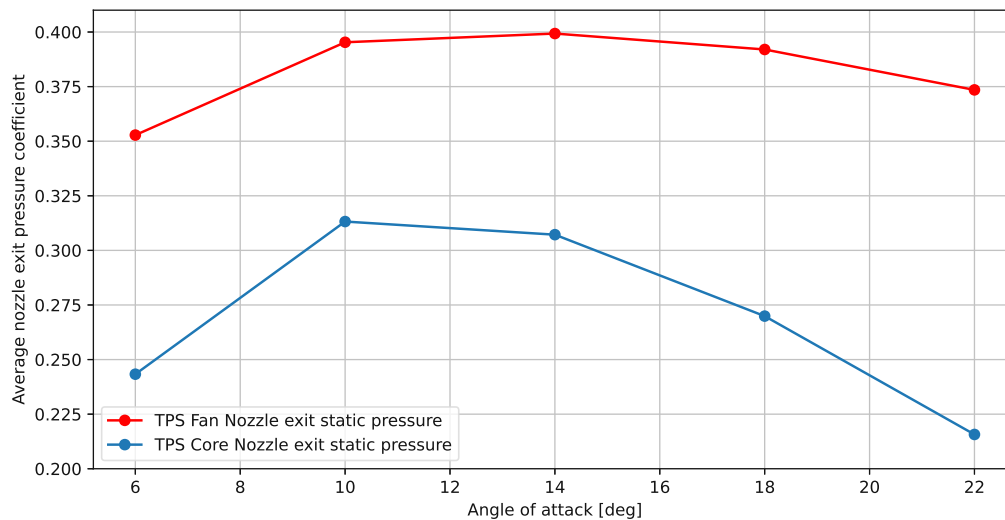


Figure 4.3: Area averaged nozzle exit pressure coefficient for a TPS engine at a FPR of 1.3 (Case 2)

The general trend is similar to that shown in Figure 4.1, with an initial rise that reaches its maximum at around 14 deg AoA, followed by a drop off towards higher AoAs. In this particular TPS model, the core nozzle experiences higher pressure fluctuations than the fan nozzle. The absolute pressure coefficients at the nozzles are different compared

to the TFN model; however, the changes of the pressure coefficients compared to the configuration at  $\alpha = 6deg$  can be compared. This is shown in Figure 4.4.

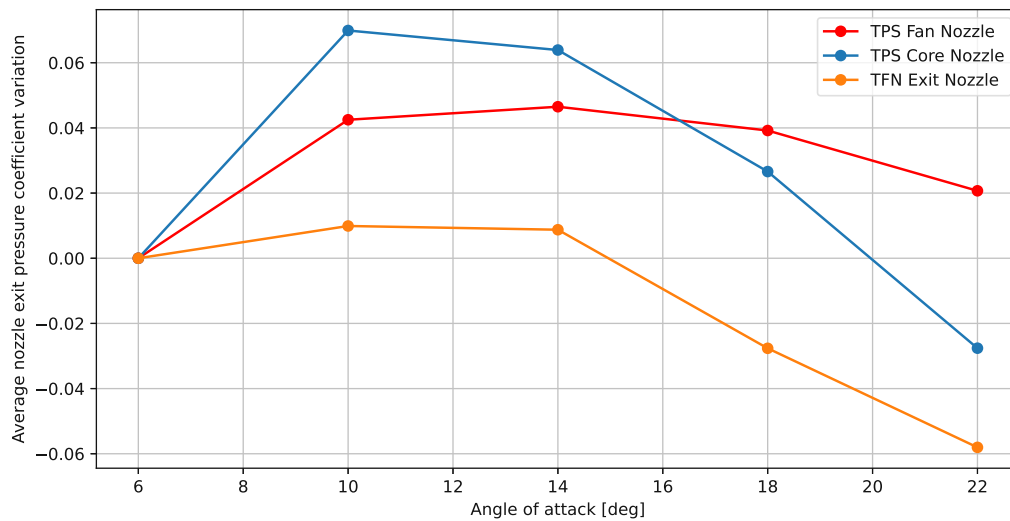


Figure 4.4: Change of installed nozzle exit pressure coefficient compared to  $\alpha = 6deg$  (Case 2)

It can be seen that the TPS model generally shows a larger sensitivity to AoA variations than the TFN model. While both reach their maximum pressure coefficients at AoAs of 10 - 14 deg, the TPS model achieves  $c_P$  values of around 0.045 higher for the fan nozzle, and 0.07 higher for the core nozzle. This is contrasted with the TFN, which achieves its maximum of around 0.01 and actually drops below the pressure coefficient of that at  $\alpha = 6deg$  at higher AoAs.

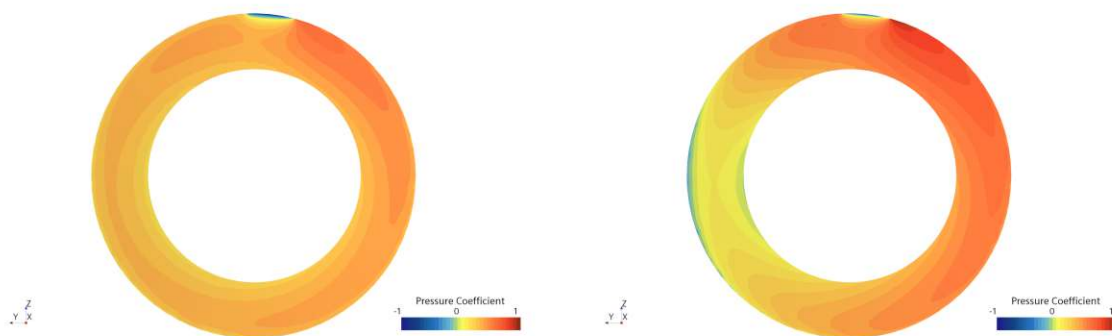


Figure 4.5: Fan nozzle exit pressure coefficient at  $\alpha = 6deg$  (Case 2.1, left) and  $\alpha = 22deg$  (Case 2.5, right)

Figure 4.5 shows that the TPS fan nozzle also exhibits the pressure field asymmetry observed in 4.1. However, the pressure increase for higher AoAs still seems to be stronger

than for a TFN, especially around the upper inboard side of the fan nozzle. A possible explanation for the increased sensitivity lies within the interaction of the fan jet stream with the flap configuration. Due to the increased local dynamic pressure, the fan stream introduces a stronger pressure field ahead of the flaps. At higher AoAs, the jet experiences a stronger impingement by the flaps, as can be seen in Figure 4.6.

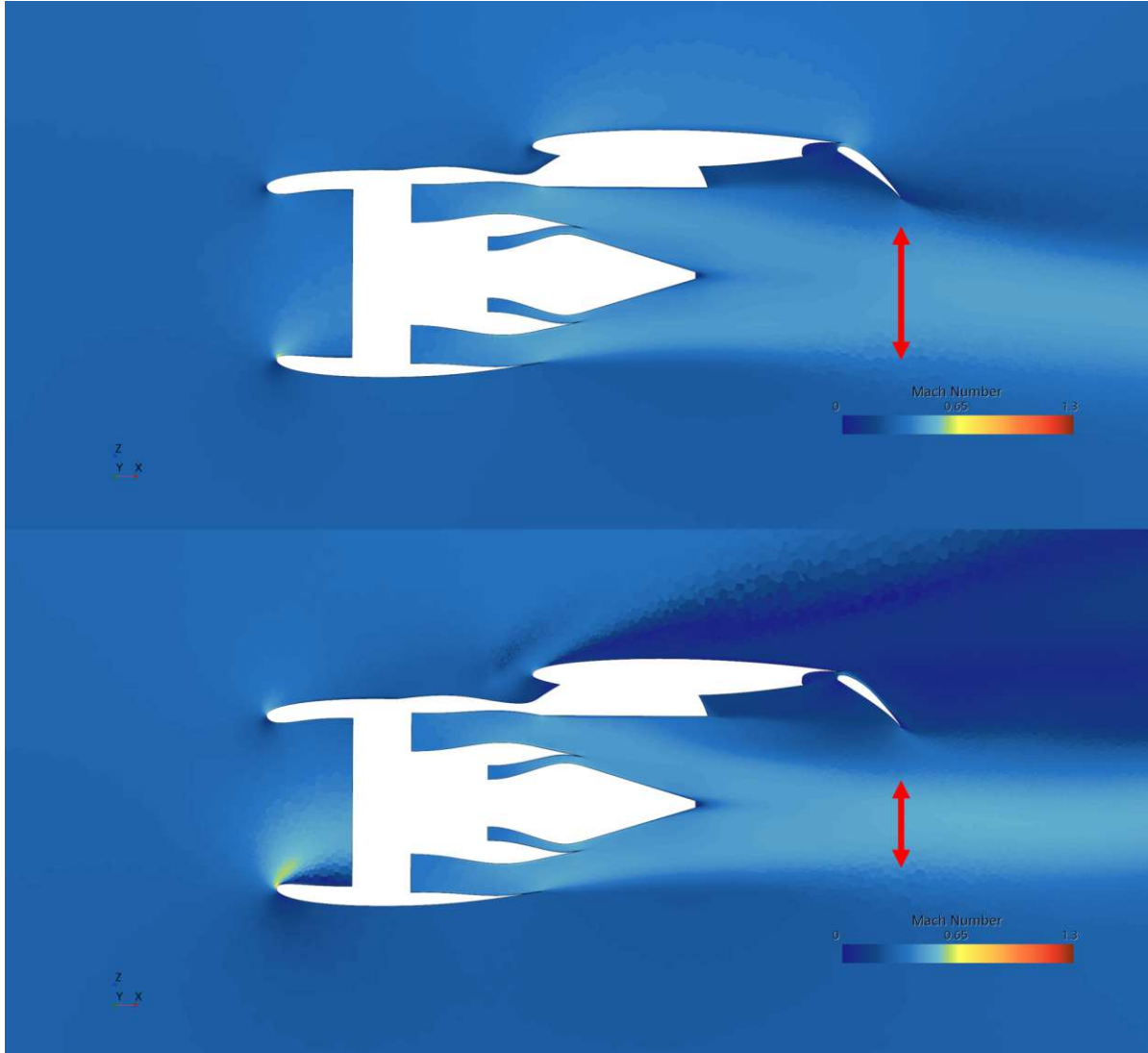


Figure 4.6: Local Mach number at  $\alpha = 6deg$  (Case 2.1, top) and  $\alpha = 22deg$  (Case 2.5, bottom)

### 4.3 Impact of thrust rating

As the TPS increases the total pressure, the impact of different thrust ratings has to be assessed. The thrust rating is adjusted by varying the FPR, which impacts the

boundary conditions of the CFD model, as well as the thrust calculated by the analytical TPS model. Figure 4.7 shows the pressure coefficients for FPR values from 1.0 to 1.5, evaluated at an AoA of 10 deg.

Case 3 - TPS FPR Sweep					
Case	Engine Geometry	FPR	HL Device Configuration	AoA	Mach number
3.1	TPS	1.0	LDG	10 deg	0.3
3.2	TPS	1.1	LDG	10 deg	0.3
3.3	TPS	1.2	LDG	10 deg	0.3
3.4	TPS	1.3	LDG	10 deg	0.3
3.5	TPS	1.4	LDG	10 deg	0.3
3.6	TPS	1.5	LDG	10 deg	0.3

Table 4.6: CFD Simulation parameters for analysis of FPR impact on suppression effects on a TPS

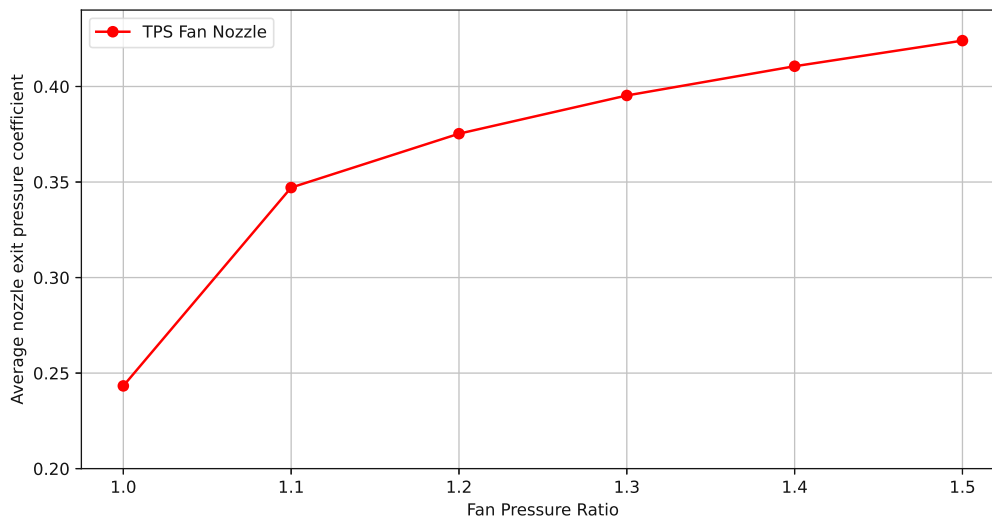


Figure 4.7: Fan nozzle static pressure coefficient for different FPR values (Case 3)

The relationship between FPR and Fan Nozzle exit pressure shows a clear relationship, with increasing FPRs resulting in increased pressure coefficients. The static pressure increase is fairly even across the section. The asymmetry observed during the AoA variations does not seem to be particularly affected by the FPR, with higher FPRs only creating a slight shift of the pressure increase towards the inboard upper part of the section. This can be seen in Table 4.7.

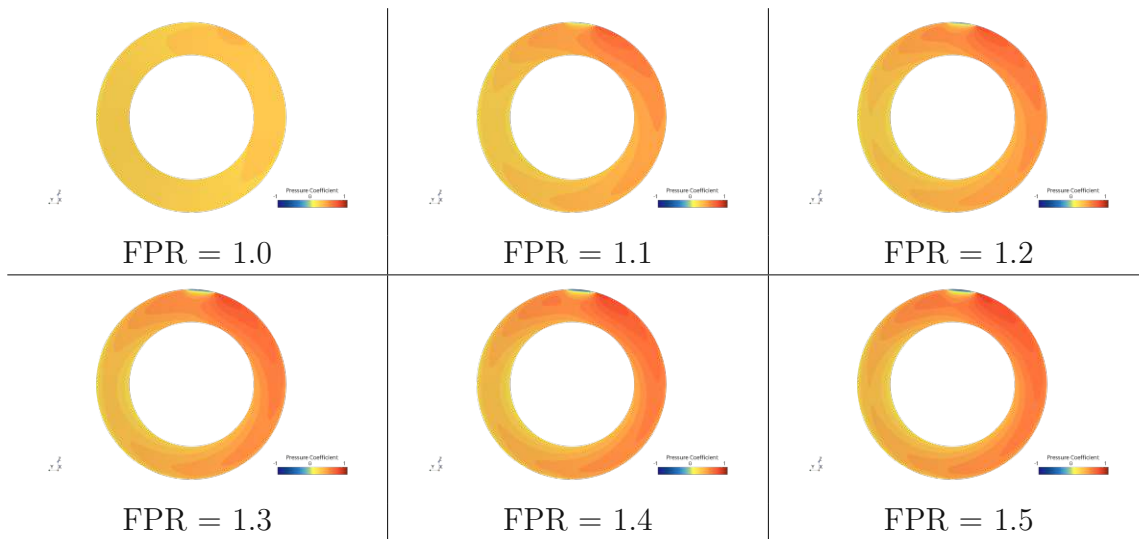


Table 4.7: Fan nozzle exit pressure coefficients for various FPRs (Case 3)

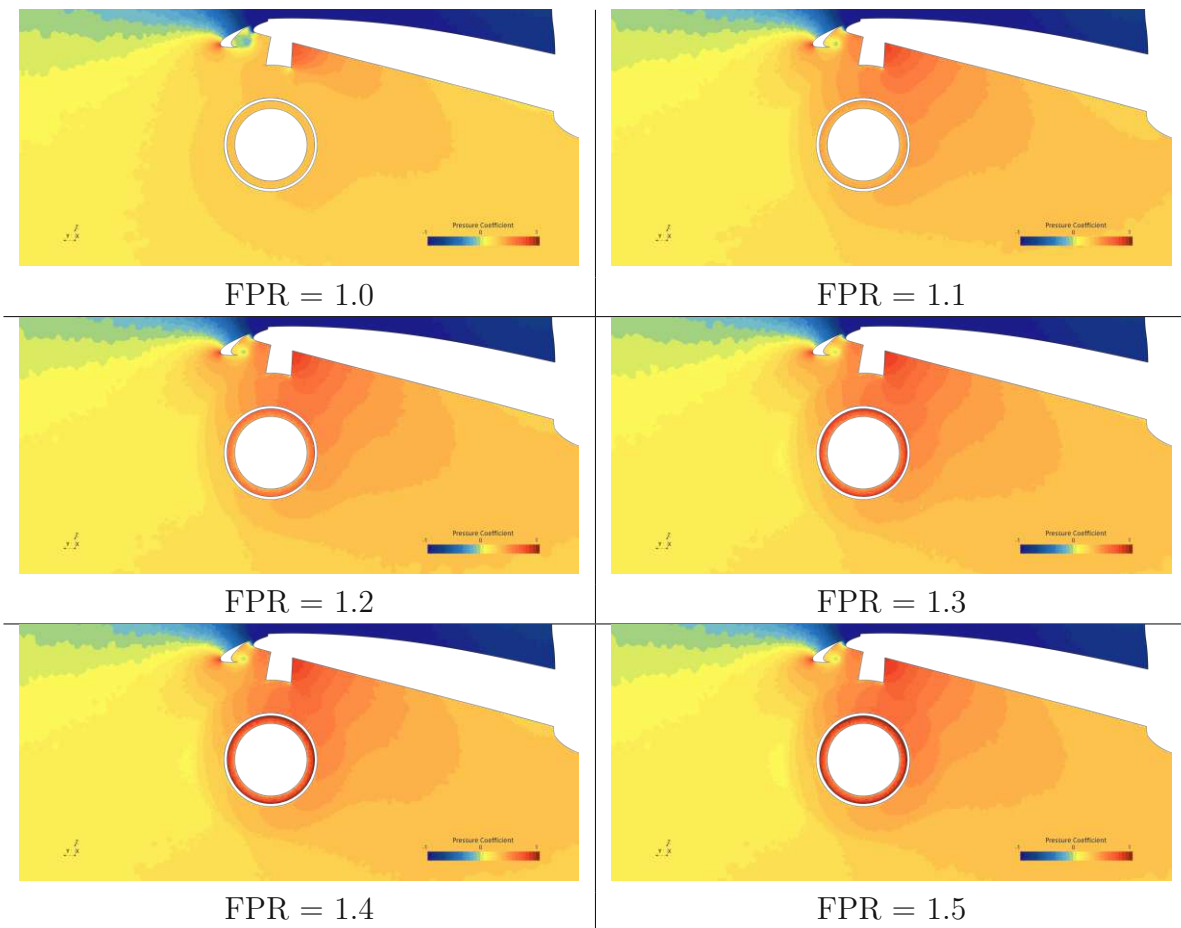


Table 4.8: Static pressure field behind the engine for various FPRs (Case 3)

Unlike increasing the AoA, increasing the FPR does not create the low pressure field on the outboard side of the engine nacelle. Instead, the pressure field becomes stronger behind the engine, increasing more towards inboard end. This indicates that the flap configuration could have a profound impact on the interaction with the engine jet stream. This can be seen in Table 4.8.

The increased increased pressure coefficient would indicate a larger effect of flow suppression for engines with higher FPRs. However, as shown in section 2.5, flow suppression has a generally reduced impact for engines with higher FPRs. Thus, it is not immediately clear how increased FPRs affect mass flow rates.

Remembering Equation 2.47:

$$\Delta C_{D,supp} = \frac{W_{PR}}{W_{FNPR}} - 1 \quad (4.2)$$

with  $PR = FNPR \cdot \frac{P_0}{P_{19,ACT}}$ , the effect of both the static pressure at the nozzle  $P_{19,ACT}$  as well as the FNPR can be evaluated for different FPRs. This combined set of data can be seen in Figure 4.8:

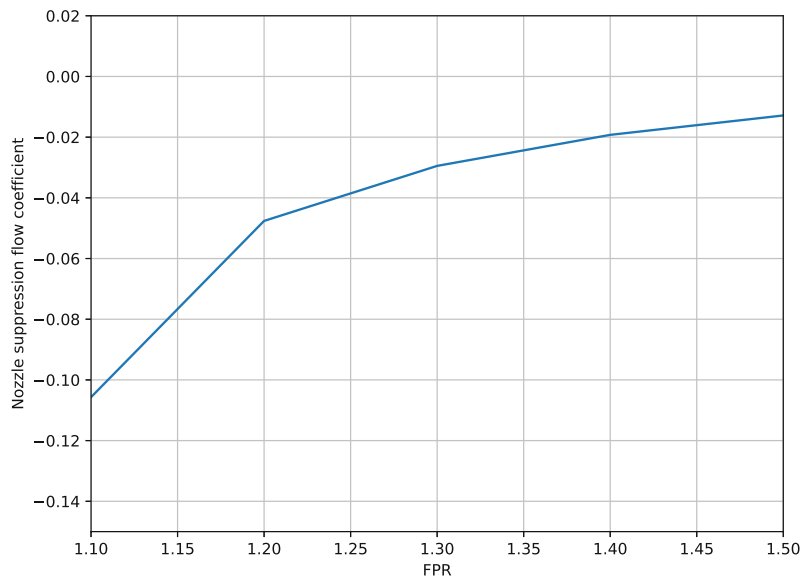


Figure 4.8: Nozzle suppression flow coefficient for various FPRs accounting for pressure field variations

It can be seen that at lower FPRs flow suppression still causes a larger bias error than at higher FPRs, albeit with a smaller difference than before. It should be noted that the exact shape of the curve is both heavily dependent on the engine model, engine parameters and the high-lift configuration of the aircraft. For a different aircraft, the

shape may be different. Nonetheless, in the case of this particular TPS on the CRM-HL, nozzle suppression coefficients are still higher for lower FPRs.

## 4.4 Improvements to the book keeping strategy

As shown in previous sections, the current method of book keeping has flaws, particularly for engines with low FPRs. As the direction for engine and airframe development appears to continue its trend towards high bypass, low FPR engines, the method needs to be adjusted in order to minimize systematic errors.

In 2.5 the error was demonstrated to be caused by an inaccurate mass flow determination methodology, relying on the assumption of nozzle exit static pressure for its calculation. Thus, any method must attempt to measure the mass flow directly.

As Berens et al. stated in [10], a likely solution would be to measure the static pressure directly at the fan nozzle (Station 19). This would be advantageous as its measurement would directly tie into the existing methodology, requiring few adjustments of the equations. However, this method has a few drawbacks. First off, the fan nozzle is a thin section, thus providing accurate measurements locally can be difficult. Additionally, as shown in 4.1, the pressure field around the fan nozzle is subject to large local variations, both radially as well as from inboard to outboard relative to the aircraft fuselage. This requires a large amount of pressure taps to be placed on both the inside as well as the outside wall, with close circumferential spacing to capture the asymmetric flow field. Thus, this method is not recommended.

An improvement to the method is made by shifting the mass flow measurement point further upstream behind the fan stage (Station 15) [10]. Measuring here alleviates the issue of the thin mechanical structure towards the tips. Additionally, the upstream position reduces the pressure field variations introduced by the external flow around the engine, leading to reduced requirements for the circumferential measurement resolution. A comparison is shown in Table 4.9:

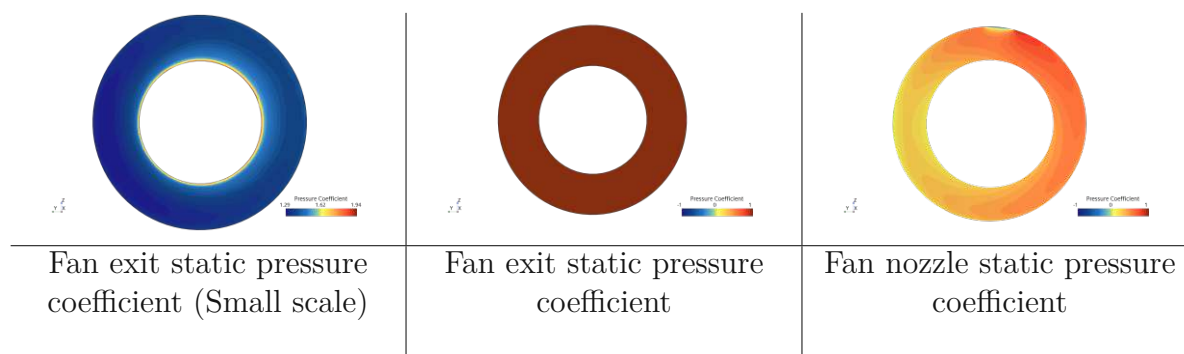


Table 4.9: Pressure coefficients for Case 2.3 right behind the fan stage (Fan Exit) and the fan nozzle

As can be seen, the asymmetry that affects measurements towards the fan nozzle is significantly reduced at the fan stage exit plane at station 15. Even viewing the pressure field at a very tight scale reveals only a very mild up-inboard shift of the pressure field. Thus, it is recommended as the preferred approach for determining thrust and drag for high bypass ratio engines.

That being said, the homogeneity to the result is also a function of the engine model being chosen. As the boundary condition specifies a constant mass flow across the fan exit face, the pressure field will numerically be constraint to remain even as well. This is not trivial on a real turbofan engine and therefore needs to be cross-checked for all applications, with circumferential pressure measurements still being strongly recommended.

In this particular case, there is also a local increase in pressure close to the inside of the fan exit stage plane. This appears to be an artifact caused by the presence of distorted prism layer cells close to the surface which create a local instability in the numerical solution, particularly when in proximity to a mass flow outlet.

# 5 Conclusions and recommendations

With the increasing importance of fuel efficiency in commercial aircraft, the development of high bypass ratio engines have gained momentum in recent years. The increased sensitivity of high bypass ratio engines to airframe integration has thus become a more relevant topic, with the effect the engine has on the airframe performance being the subject of various research. However, the impact of installation effects on engine performance and the methods associated with validating its thrust during flight have been less studied. The following chapters aim to summarize the findings of this work and provide recommendations for future research and development.

## 5.1 Conclusions

Following the thrust-drag book keeping guidelines from SAE1703A, the net thrust from an engine during flight can be estimated using flow measurements behind the fan stage. This technique relies on the assumption of freestream static pressure at the fan nozzle, which, as has been shown, is not necessarily a correct assumption. The increased nozzle exit pressure leads to nozzle suppression, shifting the engine behaviour towards higher pressure ratios and reduced mass flow. Due to the assumed freestream static pressure at the fan nozzle exit, legacy approaches do not capture this mass flow reduction, resulting in an over prediction of engine thrust - and by extension, airframe drag when performing flight testing. This effect has been shown to be significantly more prominent for engines with low fan pressure ratios, which for a given target thrust level require a higher bypass ratio.

CFD analysis has shown that there is a significant amount of airframe-induced engine suppression, which is particularly strong for a deployed high-lift configuration. Increasing the angle of attack of the aircraft shows an initial increase in nozzle flow suppression, followed by a drop at very high angles of attack. This effect is accompanied by a strong asymmetry in the fan nozzle plane pressure field, with a drop in pressure towards the outboard side of the engine. This effect has been shown to be caused by outwash generated from the airframe inducing a lateral angle of attack on the engine, as well as the side of the engine curving the airflow, leading to a drop in pressure. This drop does not occur at the inboard side of the engine due to the sweep of the wing blocking the air path.

Analysing the differences between a TPS and a TFN model shows a very similar behaviour between the two engine configurations, with the same rise-and-drop shape of the fan nozzle exit pressure field. In this particular implementation of a TPS, the sensitivity

to angle of attack variations is generally higher, with a stronger increase towards the peak due to the presence of jet effects.

Assessing the jet effect in isolation, the TPS shows a consistent increase in fan nozzle pressure for increased fan pressure ratios, as the total pressure behind the fan stage increases. Computing the nozzle suppression flow coefficients shows that despite this pressure increase for higher FPRs, the increased sensitivity to nozzle suppression effects at low FPRs still results in engines with low FPRs exhibiting larger bias errors and mass flow reductions.

## 5.2 Recommendations

As the level of fan nozzle suppression is sufficient to have a noticeable impact on the engine operation, the thrust-drag book keeping must account for this phenomenon. The methodology can be altered to add an additional point of static pressure measurement which removes the assumption of ambient static pressure at the fan nozzle. As a result, the mass flow rate is captured correctly. The location of the additional static pressure measurement should be after the fan stage, as the mechanical implementation is simpler with reduced circumferential pressure variations compared to the position at the fan nozzle.

The modelling strategy for the TPS engine can also be improved. The current model fixes the mass flow without taking the surrounding flow into account. Additionally, the assumption of homogeneous flow around the core and nozzle exit is not ideal and can be improved using either existing engine data to provide a spatially corrected boundary condition for the fan and core outlet, or a more detailed engine model that features moving fan blades.

With future engines set to increase the bypass ratio even further, more attention should be placed on the installation effects when deployed on an airframe. The effect of nozzle suppression extends beyond just a bias error within the thrust-drag book keeping - as the mass flow gets reduced, the nozzle operation alters, which becomes more impactful with lower fan pressure ratios. The reduced flow rate also shifts the Mach number for critical nozzle flow towards higher freestream Mach numbers. Thus, future testing procedures should consider testing of the engine in its installed configuration.

# List of Figures

1.1	Crude oil price development from 1960 to 2025 (Source: [7]) . . . . .	5
1.2	Turbofan engine and nacelle installation SFC increments (Source: [9]) . .	6
2.1	Station positions and labels for a turbofan engine (Source: [12]) . . . . .	8
2.2	Control positions for a single - stream engine (Source: [12]) . . . . .	9
2.3	Control positions for a dual - stream engine (Source: [12]) . . . . .	12
2.4	Engine operation curve for an engine with nozzle flow suppression and without nozzle flow suppression on a generic high bypass ratio engine . .	17
2.5	Thrust-drag book keeping error demonstrated on a generic high bypass ratio engine . . . . .	17
2.6	Nozzle suppression flow coefficients for various nozzle exit static pressure coefficients and FNPRs . . . . .	18
3.1	Leading edge modifications made to CRM-HL vs. CRM-HS (Source: [16])	21
3.2	Geometry comparison of ONERA F1 model (yellow) against standard CRM-HL model (grey) . . . . .	21
3.3	Detailed view of flap track fairings and slat brackets . . . . .	22
3.4	Changes from ONERA F1 geometry to final CFD geometry . . . . .	22
3.5	Detailed view of outboard slat bracket simplifications . . . . .	23
3.6	Mounted TPS on CRM-HL . . . . .	24
3.7	Detail view of TPS on CRM-HL . . . . .	24
3.8	Comparison of TFN geometry to TPS geometry . . . . .	25
3.9	Comparison of TFN geometry to TPS geometry from side view . . . . .	25
3.10	Comparison of TFN geometry to TPS geometry from bottom view . . . . .	26
3.11	Boundary condition regions for the TPS model (Yellow: Inlets, Green: Outlet) . . . . .	28
3.12	Velocity field around the TPS engine at $\alpha = 10deg$ and $FPR = 1.3$ . . . .	29
3.13	Refinement volumes . . . . .	30
3.14	Wall $y+$ values for the first cell . . . . .	31
3.15	Mesh slice at the trailing edge . . . . .	31
3.16	Mesh slice at symmetry plane . . . . .	32
3.17	Lift Coefficient grid convergence study . . . . .	33
3.18	Drag Coefficient grid convergence study . . . . .	33
3.19	Average Pressure Coefficient at Nacelle Exit Plane grid convergence study	34
3.20	Cell count for Grid convergence study . . . . .	34
3.21	Grids for CpC values of 6.25 (top left), 12.5 (top right), 25 (bottom left), 50 (bottom right) . . . . .	35
3.22	Wing top surface mesh for finest resolution . . . . .	36
3.23	Wing bottom surface mesh for finest resolution . . . . .	36

3.24	Comparison of lift coefficient between CFD and wind tunnel data . . . .	37
3.25	Comparison of drag coefficient between CFD and wind tunnel data . . . .	37
3.26	Results from Siemens [21] for lift and drag coefficients of the CRM-HL ONERA F1 wind tunnel test geometry in CFD . . . . .	38
4.1	Area averaged nozzle exit pressure coefficient for an installed TFN engine (Case 1) . . . . .	40
4.2	Nozzle suppression flow coefficients for a TFN engine (Case 1) . . . . .	42
4.3	Area averaged nozzle exit pressure coefficient for a TPS engine at a FPR of 1.3 (Case 2) . . . . .	44
4.4	Change of installed nozzle exit pressure coefficient compared to $\alpha = 6deg$ (Case 2) . . . . .	45
4.5	Fan nozzle exit pressure coefficient at $\alpha = 6deg$ (Case 2.1, left) and $\alpha = 22deg$ (Case 2.5, right) . . . . .	45
4.6	Local Mach number at $\alpha = 6deg$ (Case 2.1, top) and $\alpha = 22deg$ (Case 2.5, bottom) . . . . .	46
4.7	Fan nozzle static pressure coefficient for different FPR values (Case 3) . .	47
4.8	Nozzle suppression flow coefficient for various FPRs accounting for pressure field variations . . . . .	49

# List of Tables

3.1	TPS boundary conditions for different thrust ratings . . . . .	29
4.1	CFD Simulation parameters for analysis of AoA impact on suppression effects on a TFN . . . . .	39
4.2	Comparison of the installed nacelle exit pressure field at various angles of attack (Case 1) . . . . .	40
4.3	Pressure coefficient (left) and velocity vector (right) field around the installed engine nacelle at $\alpha = 22deg$ (Case 1.5) . . . . .	41
4.4	Pressure field comparison for $\alpha = 6deg$ and $\alpha = 22deg$ . . . . .	43
4.5	CFD Simulation parameters for analysis of AoA impact on suppression effects on a TPS . . . . .	44
4.6	CFD Simulation parameters for analysis of FPR impact on suppression effects on a TPS . . . . .	47
4.7	Fan nozzle exit pressure coefficients for various FPRs (Case 3) . . . . .	48
4.8	Static pressure field behind the engine for various FPRs (Case 3) . . . . .	48
4.9	Pressure coefficients for Case 2.3 right behind the fan stage (Fan Exit) and the fan nozzle . . . . .	50

# Bibliography

- [1] D. Scholz, "Umweltschutz in der Luftfahrt – Hintergründe und Argumente zur aktuellen Diskussion," HAW Hamburg, Tech. Rep., 2021.
- [2] D. Lee, *Transport impacts on atmosphere and climate: Aviation*, 2009. DOI: 10.1016/j.atmosenv.2009.06.005.
- [3] International Energy Agency, *World air passenger traffic evolution, 1980-2020*, Last accessed on 15 November 2025. [Online]. Available: <https://www.iea.org/data-and-statistics/charts/world-air-passenger-traffic-evolution-1980-2020>.
- [4] ICAO, *World Aviation and the World Economy*, Last accessed on 01 December 2025, 2023. [Online]. Available: [https://www2023.icao.int/sustainability/pages/facts-figures\\_worldconomydata.aspx](https://www2023.icao.int/sustainability/pages/facts-figures_worldconomydata.aspx).
- [5] European Commission, *Communication from the commission to the european parliament, the european council, the council, the european economic and social committee and the committee of the regions*, 2019.
- [6] EUROCONTROL, *Aircraft operating costs*, Last accessed 06 June 2025, 2022. [Online]. Available: [https://ansperformance.eu/economics/cba/standard-inputs/latest/chapters/aircraft\\_operating\\_costs.html](https://ansperformance.eu/economics/cba/standard-inputs/latest/chapters/aircraft_operating_costs.html).
- [7] Statista, *Average annual OPEC crude oil price from 1960 to 2025*, Last accessed on 10 June 2025, 2025. [Online]. Available: <https://www.statista.com/statistics/262858/change-in-opec-crude-oil-prices-since-1960/>.
- [8] C. S. Campomanes, "External flow effects in the engine/airframe integration testing technique - A new thrust/drag bookkeeping approach at the German-Dutch wind tunnels," M.S. thesis, TU Delft, 2017.
- [9] SAE INTERNATIONAL, *AIR5450*, 2014.
- [10] M. Berens, M. de Rosa Jacinto, and B. Gerl, "Simulation of turbofan engine flow suppression effects," in *Conference Proceedings of the DLRK 2022*, 2022. DOI: 10.25967/570424.
- [11] W. de Wolf, "Workshop on Aspects of Airframe Engine Integration for Transport Aircraft," in *Possibilities and limitations of VHBR and UHBR turbofan simulations in engine/airframe integration wind tunnel experiments*, 1996.
- [12] SAE INTERNATIONAL, *AIR1703A*, 2017.
- [13] M. B. Rivers, *NASA Common Research Model: A History and Future Plans*, Last accessed on 30 June 2025, 2017. DOI: 10.2514/6.2019-3725. [Online]. Available: <https://ntrs.nasa.gov/api/citations/20200002395/downloads/20200002395.pdf>.

- [14] J. C. Vassberg, M. A. DeHaan, S. M. Rivers, and R. A. Wahls, *Development of a Common Research Model for Applied CFD Validation Studies*, Last accessed on 30 June 2025, 2012. DOI: 10.2514/6.2008-6919. [Online]. Available: [https://commonresearchmodel.larc.nasa.gov/wp-content/uploads/sites/7/2015/04/AIAA-2008-6919-Vassberg\\_compliant2.pdf](https://commonresearchmodel.larc.nasa.gov/wp-content/uploads/sites/7/2015/04/AIAA-2008-6919-Vassberg_compliant2.pdf).
- [15] D. S. Lacy and A. J. Sclafani, *Development of the High Lift Common Research Model (HL-CRM): A Representative High Lift configuration for Transonic Transports*, Last accessed on 30 June 2025, 2016. DOI: 10.2514/6.2016-0308. [Online]. Available: [https://commonresearchmodel.larc.nasa.gov/wp-content/uploads/sites/7/2023/02/AIAA2016-0308\\_CRMHL.pdf](https://commonresearchmodel.larc.nasa.gov/wp-content/uploads/sites/7/2023/02/AIAA2016-0308_CRMHL.pdf).
- [16] D. Lacy and A. M. Clark, *Definition of Initial Landing and Takeoff Reference Configurations for the High Lift Common Research Model (CRM-HL)*, Last accessed on 02 July 2025, 2020. DOI: 10.2514/6.2020-2771. [Online]. Available: <https://commonresearchmodel.larc.nasa.gov/wp-content/uploads/sites/7/2023/02/AIAA-2020-2771-Reference-Configuration.pdf>.
- [17] A. Evans, D. Lacy, I. Smith, and M. Rivers, *Test Summary of the NASA Semi-Span High Lift Common Research Model at the QinetiQ 5-Metre Low-Speed Wind Tunnel*, Last accessed on 02 July 2025, 2020. DOI: 10.2514/6.2020-2770. [Online]. Available: <https://commonresearchmodel.larc.nasa.gov/wp-content/uploads/sites/7/2023/02/AIAA-2020-2770.pdf>.
- [18] S. Mouton, G. Charpentier, and A. Lorenski, *Test Summary of the Full-Span High-Lift Common Research Model at the ONERA F1 Pressurized Low-Speed Wind Tunnel*, Last accessed on 02 July 2025, 2023. DOI: 10.2514/6.2023-0823. [Online]. Available: <https://commonresearchmodel.larc.nasa.gov/wp-content/uploads/sites/7/2023/02/AIAA-2023-0823.pdf>.
- [19] R. Djeddi, *HLPW5: Summary of Unstructured Mesh Generation Efforts with Fidelity Pointwise for Fixed-Grid RANS Analyses*, Last accessed on 03 July 2025, 2024. DOI: 10.2514/6.2025-0681. [Online]. Available: [https://hiliftpw.larc.nasa.gov/Workshop5/WorkshopPresentations/HLPW5\\_Meshing\\_Overview\\_Fidelity\\_Pointwise.pdf](https://hiliftpw.larc.nasa.gov/Workshop5/WorkshopPresentations/HLPW5_Meshing_Overview_Fidelity_Pointwise.pdf).
- [20] A. Wick and R. Hooker, *Overview of Grids Created with HeldenMesh for HLPW5 Meshing Lessons Learned*, Last accessed on 03 July 2025, 2024. DOI: 10.2514/6.2025-0683. [Online]. Available: [https://hiliftpw.larc.nasa.gov/Workshop5/WorkshopPresentations/HLPW5\\_Meshing\\_Overview\\_HeldenMesh.pdf](https://hiliftpw.larc.nasa.gov/Workshop5/WorkshopPresentations/HLPW5_Meshing_Overview_HeldenMesh.pdf).
- [21] J. Hanke and C. Nelson, “Fixed Grid RANS Results using Simcenter STAR-CCM+ for the 5th AIAA CFD High Lift Prediction Workshop,” in *HLPW-5*, 2024.
- [22] C. Wimmer, “Effects of Isolated and Installed Turbofan Engine Nozzle Flows on Nozzle Pressure Coefficients for Various Thrust Ratings,” M.S. thesis, TU Wien, 2025.
- [23] AIAA Applied Aerodynamics Technical Committee, *High Lift Prediction Workshop 5*, <https://hiliftpw.larc.nasa.gov/> [Accessed: 15.04.2025], 2024.

- [24] Siemens, *Best Practices: External Aerodynamics for Aerospace Applications*, 2018.
- [25] R. Rudnik, A. Ronzheimer, C.-C. Rossow, and H. Hoheisel, "Investigation of the flowfield around an isolated engine with fan and core jet," *AGARD CP498*, 1992.
- [26] R. Rudnik, C.-C. Rossow, and H. von Geyr, "Numerical simulation of engine/airframe integration for high-bypass engines," *Aerospace Science and Technology* 6, 2001. DOI: 10.1016/S1270-9638(01)01139-7.